

Shape transformations of vesicles: Phase diagram for spontaneous-curvature and bilayer-coupling models

Udo Seifert,* Karin Berndl, and Reinhard Lipowsky†

Sektion Physik der Universität München, Theresienstrasse 37, 8000 München 2, Federal Republic of Germany

(Received 1 October 1990)

Vesicle shapes of low energy are studied for two variants of a continuum model for the bending energy of the bilayer: (i) the spontaneous-curvature model and (ii) the bilayer-coupling model, in which an additional constraint for the area difference of the two monolayers is imposed. We systematically investigate four branches of axisymmetric shapes: (i) the prolate-dumbbell shapes; (ii) the pear-shaped vesicles, which are intimately related to budding; (iii) the oblate-discocyte shapes; and (iv) the stomatocytes. These branches end up at limit shapes where either the membrane self-intersects or two (or more) shapes are connected by an infinitesimally narrow neck. The latter limit shape requires a certain condition between the curvatures of the adjacent shape and the spontaneous curvature. For both models, the phase diagram is determined, which is given by the shape of lowest bending energy for a given volume-to-area ratio and a given spontaneous curvature or area difference, respectively. The transitions between different shapes are continuous for the bilayer-coupling model, while most of the transitions are discontinuous in the spontaneous-curvature model. We introduce trajectories into these phase diagrams that correspond to a change in temperature and osmotic conditions. For the bilayer-coupling model, we find extreme sensitivity to an asymmetry in the monolayer expansivity. Both models lead to different predictions for typical trajectories, such as budding trajectories or oblate-stomatocyte transitions. Our study thus should provide the basis for an experimental test of both variants of the curvature model.

I. INTRODUCTION

Lipid bilayers form closed surfaces or vesicles in aqueous solution in order to prevent any contact between the hydrocarbon chains of the lipid molecules and the water [1–3]. These vesicles can be isolated and studied in a controlled way. Three classes of experiments have been performed so far: (i) Transformations between a wide variety of different shapes which include prolate and oblate ellipsoids, biconcave discocytes, and cup-shaped stomatocytes can be induced, e.g., by changing the temperature or the osmotic conditions [4–6]. Recently, the phenomenon of budding, i.e., the expulsion of a smaller vesicle out of a larger one, has attracted a lot of interest [7]. (ii) For quasispherical vesicles the long-wavelength fluctuations which are thermally excited bending modes have been investigated by light microscopy and video recording [8–11]. (iii) Micropipet aspiration techniques yield information about thermal and mechanical properties and allow the study of the mutual adhesion of giant vesicles [12–14].

These experiments tend to confirm the theoretical idea that the shape of a vesicle is mainly determined by bending elasticity and, thus, by curvature. The theoretical work on these different conformations of vesicles is based on continuum models for the bending elasticity [15–17]. In these models, the membrane is viewed as a two-dimensional surface embedded in three-dimensional space. Its elastic properties are described by two bending rigidities. Several studies applied these concepts in order to (i) calculate vesicle shapes [18–25], (ii) analyze the flicker spectrum of the bending modes [26,27], and (iii)

calculate the shapes and phase diagram of bound vesicles [28,29].

Two variants of a continuum description have been introduced and studied: (i) the spontaneous-curvature model [16] and (ii) the bilayer-coupling model [24,25]. By minimization of the bending energy for given area and enclosed volume, Deuling and Helfrich [18] obtained a rich catalog of axisymmetric vesicle shapes for the spontaneous-curvature model. Several further studies of this model were devoted to modifications of the numerical algorithm or the investigation for particular values of the parameters [19–23]. However, the systematics of the phase diagram, which is determined by the shape of lowest energy, has not been elucidated so far.

In a somewhat different approach, Svetina and Zeks [24,25] combined bending elasticity with the bilayer-coupling hypotheses [17,30]. In this approach, the two monolayers are considered to be coupled at a fixed distance but are not allowed to exchange lipid molecules. This leads to an additional constraint which can be incorporated into the continuum model. The corresponding phase diagram has already been partially investigated [25].

In this paper, we systematically study axisymmetric shapes which minimize the bending energy and determine the phase diagram for both the spontaneous-curvature and the bilayer-coupling model. We find a new branch of shapes, the pear-shaped vesicles, and limit shapes consisting of several spheres connected by narrow necks. The occurrence of these shapes is intimately related to the budding phenomenon.

Although the bilayer-coupling and the spontaneous-

curvature model are related via a Legendre transformation, the corresponding phase diagrams are quite different. Therefore, our results make it possible to test both models experimentally since they lead to different predictions for the sequence of shape transformations. In particular, all transitions found in the bilayer-coupling model are continuous while most of the transitions in the spontaneous-curvature model are discontinuous.

In order to facilitate the comparison with experiments, we introduce trajectories into the phase diagrams for two experimentally convenient parameters, the temperature and the osmotic conditions. For variations in the temperature, our theory shows extreme sensitivity of the sequence of shape transformations to a small asymmetry in the thermal expansivity of the two monolayers [31]. This provides an explanation for the variety of shape transformations which have been observed recently even in simple binary systems consisting of one lipid and water [31].

This paper is organized as follows: In Sec. II we define both models and introduce our notation. In Sec. III we derive the shape equations in a certain parametrization and discuss the branches of stationary shapes. In Secs. IV and V we discuss the phase diagram for the bilayer-coupling model and the spontaneous-curvature model, respectively. Trajectories in these phase diagrams are then calculated in Sec. VI as a function of temperature and osmotic conditions. A summary concludes the paper in Sec. VII.

II. BENDING ENERGY AND CURVATURE MODELS

A. Spontaneous-curvature model

In the spontaneous-curvature model of Helfrich, the bending energy of the vesicle with surface area A and volume V is given by [16]

$$F_b \equiv (\kappa/2) \oint dA (C_1 + C_2 - C_0)^2 + \kappa_G \oint dA C_1 C_2 . \quad (2.1)$$

The variables C_1 and C_2 denote the two principal curvatures, while the spontaneous curvature C_0 is phenomenologically introduced in order to account for a possible asymmetry of the bilayer. The second term gives the integrated Gaussian curvature which is constant for topologically equivalent shapes. In this paper we will focus on shapes which have the same topology as a sphere and, thus, we will omit this term in the remainder.

The shape of a vesicle is now determined by the minimum of F_b for a given area A and a given volume V . These constraints are incorporated via Lagrange multipliers Σ and P . The shape equations are then obtained from

$$\delta F \equiv \delta(F_b + \Sigma A + PV) = 0 . \quad (2.2)$$

where δ denotes variation with respect to the shape of the vesicle and Σ and P are adjusted in order to guarantee the prescribed area and volume.

B. Bilayer-coupling model

The bilayer-coupling model is based on the assumption that the two monolayers do not exchange lipid molecules, i.e., area, on experimentally relevant time scales. The bending energy of the vesicle is taken to be

$$G_b \equiv (\kappa/2) \oint dA (C_1 + C_2)^2 , \quad (2.3)$$

where the integration is over a suitably defined reference surface of the two coupled monolayers. A possible definition of the reference surface is discussed in Appendix A. The difference

$$\Delta A \equiv A^{\text{ex}} - A^{\text{in}} \quad (2.4)$$

of the areas A^{ex} and A^{in} of the exterior and interior monolayer can then be expressed by the integrated mean curvature M ,

$$M \equiv \frac{1}{2} \oint dA (C_1 + C_2) , \quad (2.5)$$

since

$$\Delta A \approx 2DM , \quad (2.6)$$

up to order D^2/A , where D denotes the distance between the two monolayers. The bilayer-coupling model requires the minimization of G_b for a given area A , for a given volume V , and a given area difference ΔA , i.e., integrated mean curvature M [24,25]. If we denote the corresponding Lagrange multipliers with Σ' , P , and Q , respectively, the shape equations derive from

$$\delta F' \equiv \delta(G_b + \Sigma' A + PV + QM) = 0 . \quad (2.7)$$

With the identifications

$$\Sigma' \equiv \Sigma + \kappa C_0^2/2 \quad \text{and} \quad Q \equiv -2\kappa C_0 , \quad (2.8)$$

one finds

$$F = F' . \quad (2.9)$$

Thus, both models lead to the same shape equations, as previously observed by Svetina and Zeks [25].

C. Consequences of the scale invariance

Any shape of the vesicle is given by a vector-valued function $\mathbf{R} = \mathbf{R}(s_1, s_2)$, where s_1 and s_2 denote suitable coordinates. The bending energies as given by (2.1) and (2.3) are invariant under the rescaling transformation

$$\mathbf{R} \rightarrow \lambda \mathbf{R} , \quad (2.10)$$

provided one transforms $\kappa \rightarrow \kappa$ and $C_0 \rightarrow C_0/\lambda$, while one has $A \rightarrow \lambda^2 A$, $V \rightarrow \lambda^3 V$, and $M \rightarrow \lambda M$. For any solution of (2.7), F' must be stationary under an infinitesimal scale transformation (2.10) with small $\lambda - 1$, which leads to [25]

$$\begin{aligned} \left. \frac{dF'}{d\lambda} \right|_{\lambda=1} = 0 &= \left. \left[\frac{dG_b}{d\lambda} \right] \right|_{\lambda=1} + \Sigma' \left. \left[\frac{dA}{d\lambda} \right] \right|_{\lambda=1} \\ &+ P \left. \left[\frac{dV}{d\lambda} \right] \right|_{\lambda=1} + Q \left. \left[\frac{dM}{d\lambda} \right] \right|_{\lambda=1} \\ &= 0 + 2\Sigma' A + 3PV + QM . \end{aligned} \quad (2.11)$$

The Lagrange parameters P , Σ' , and Q are given by the partial derivatives of G_b ,

$$P = - \left[\frac{\partial G_b}{\partial V} \right]_{A,M}, \quad (2.12a)$$

$$\Sigma' = - \left[\frac{\partial G_b}{\partial A} \right]_{V,M}, \quad (2.12b)$$

and

$$Q = - \left[\frac{\partial G_b}{\partial M} \right]_{A,V}, \quad (2.12c)$$

as found by differentiating (2.7).

III. SHAPE EQUATIONS AND STATIONARY SHAPES

A. Parametrization of vesicle shape

We restrict our search for minimal solutions to axisymmetric shapes and use as coordinates the arclength S along the contour and the azimuthal angle ϕ (see Fig. 1). The shape is then determined by the tilt angle $\psi(S)$, as defined in Fig. 1. We use moreover the coordinates X and Z , which are perpendicular and parallel to the axis of symmetry, respectively. Then, the geometrical relations

$$\dot{X} = \cos\psi, \quad (3.1a)$$

$$\dot{Z} = -\sin\psi, \quad (3.1b)$$

$$C_1 = \dot{\psi}, \quad (3.1c)$$

and

$$C_2 = \sin\psi/X \quad (3.1d)$$

are evident, where the dot denotes a derivative with respect to S . The advantage of using the parametrization $\psi(S)$ compared to $Z(X)$ is that points with infinite derivative dZ/dX are regular in this parametrization. The total energy F as given by (2.2) may now be expressed as [22]

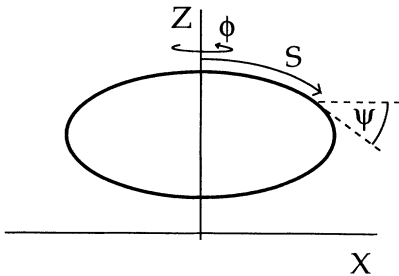


FIG. 1. Parametrization of vesicle shape. The axis of symmetry is denoted by Z . S denotes the arclength along the contour measured from the north pole of the shape and ϕ the azimuthal angle. $\Psi(S)$ is the angle between the tangent to the contour and the X axis.

$$F = 2\pi\kappa \int_0^{S_1} L(\psi, \dot{\psi}, X, \dot{X}, \gamma) dS, \quad (3.2a)$$

with the ‘‘Lagrange function’’

$$L \equiv \frac{X}{2} \left[\dot{\psi} + \frac{\sin\psi}{X} - C_0 \right]^2 + \bar{\Sigma}X + \frac{\bar{P}}{2} X^2 \sin\psi + \gamma(\dot{X} - \cos\psi) \quad (3.2b)$$

and rescaled parameters

$$\bar{P} \equiv P/\kappa \quad (3.3a)$$

and

$$\bar{\Sigma} \equiv \Sigma/\kappa. \quad (3.3b)$$

The last term in (3.2b) which involves the Lagrange parameter function $\gamma = \gamma(S)$ must be introduced since the variables ψ and X are related by (3.1a). Note that the ‘‘Hamiltonian function’’

$$H \equiv -L + \dot{\psi} \partial L / \partial \dot{\psi} + \dot{X} \partial L / \partial \dot{X} = \frac{X}{2} \left[\dot{\psi}^2 - \left[\frac{\sin\psi}{X} - C_0 \right]^2 \right] - \frac{\bar{P}}{2} X^2 \sin\psi - \bar{\Sigma}X + \gamma \cos\psi \quad (3.4)$$

is conserved, since $\partial L / \partial S = 0$.

B. Shape equations and boundary conditions

The set of Euler-Lagrange equations for F , which are the shape equations, read

$$\dot{\psi} = U, \quad (3.5a)$$

$$\dot{U} = -\frac{U}{X} \cos\psi + \frac{\cos\psi \sin\psi}{X^2} + \frac{\gamma}{X} \sin\psi + \frac{\bar{P}X}{2} \cos\psi, \quad (3.5b)$$

$$\dot{\gamma} = (U - C_0)^2/2 - \frac{\sin^2\psi}{2X^2} + \bar{P}X \sin\psi + \bar{\Sigma}, \quad (3.5c)$$

$$\dot{X} = \cos\psi. \quad (3.5d)$$

The boundary conditions for ψ and X are obvious:

$$\psi(0) = 0, \quad (3.6a)$$

$$\psi(S_1) = \pi, \quad (3.6b)$$

$$X(0) = 0, \quad (3.6c)$$

and

$$X(S_1) = 0. \quad (3.6d)$$

Since the length of the integration interval S_1 is free, the extremal conditions (2.2) lead to $H(S_1) = 0$, which implies together with (3.4) the boundary condition

$$\gamma(S_1) = 0. \quad (3.7)$$

It then follows from the conservation of H that the initial condition for γ is given by

$$\gamma(0) = H(0) = 0. \quad (3.8)$$

C. Branches of stationary shapes

We describe in Appendix B a systematic algorithm which leads in principle to a complete set of solutions of the shape equation (3.5) for given parameters $\bar{\Sigma}$, \bar{P} , and C_0 . These solutions which are the *stationary shapes* contain local minima and saddle points in the space of all shapes. Physically relevant are the local minima, while the saddle points give the activation energies for transitions between different minima. Whether a shape is a minimum or a saddle point can be investigated by a stability analysis and may depend on the particular variant of the curvature model under consideration. In this paper, we have not attempted to perform such an analysis in general. However, stability in the spherical limit is addressed in Sec. IV C below, while stability with respect to axisymmetric deformations can be investigated by a close inspection of the bifurcation structure (see Sec. V A for an example).

In the remainder of this section, we describe the systematics of the stationary shapes and those features of these shapes which hold in both variants of the curvature model. A comparison of the energy of these shapes and the available information on their stability is given in Secs. IV and V for each variant separately. The stationary shapes can be classified according to branches. Within a branch, the shape varies smoothly as a function of the parameters.

In fact, a discrete but infinite set of branches is known to exist from analytic work in which one considers small deviations from the spherical shape [32–34]. Indeed, the sphere with radius R_0 is a solution to $\delta F = 0$, if [16]

$$\bar{P}R_0^2 + (2\bar{\Sigma} + C_0^2)R_0 - 2C_0 = 0. \quad (3.9)$$

For given \bar{P} and C_0 , this relation defines two curves in the $[U(0), \Sigma]$ plane, which denote spheres for $U(0) \equiv 1/R_0 > 0$ and inverted spheres for $U(0) < 0$.

A slightly deformed sphere can be parametrized by

$$R(\theta, \phi) = R_0 + \sum_{l,m} a_{l,m} Y^{l,m}(\theta, \phi), \quad (3.10)$$

where R denotes the distance from the center of the undeformed sphere and θ and ϕ are spherical coordinates. The second variation $\delta^2 F$ vanishes for a deformation with fixed l for

$$R_0^3 \bar{P}_{c,l} = 2[l(l+1) - R_0 C_0], \quad (3.11)$$

which defines the critical pressure $\bar{P}_{c,l}$. At $\bar{P} = \bar{P}_{c,l}$, the spherical shape becomes unstable with respect to a $Y^{l,m}$ perturbation in an ensemble where the pressure instead of the volume is prescribed [32].

For $l=2$, the axisymmetric shapes that arise from the instability are prolate and oblate ellipsoids. We focus in this paper on the shapes that develop from this instability, since the ($l=2$) shapes are known to have the lowest bending energy in the vicinity of the sphere. Moreover, Peterson, [34] has found that shapes that arise from the ($l \geq 3$) instability are unstable with respect to ellipsoidal deformations (see Sec. IV C below).

We now discuss five examples for the behavior of various branches in the $[U(0), \Sigma]$ plane. Here $U(0)$ denotes

the curvature at the north pole of the shape and Σ the Lagrange multiplier for the area, respectively; compare Appendix B. These examples are displayed in Figs. 2(a)–2(e).

Example (a) with $\bar{P} > 0$ and $C_0 = 0$ [see Fig. 2(a)]. The starting point at which the prolate and oblate branches bifurcate from the sphere branch follows from (3.11) with $l=2$ and from (3.9) with $\bar{P} = \bar{P}_{c,2}$. The *prolate* branch first leads to prolate ellipsoids, which look more and more like dumbbells as one moves further along this branch. These dumbbells approach finally the shape of an (infinitely) long capped cylinder of radius R_{cyl} as $[U(0), \Sigma]$ spiral to the limit point $[U(0)_{\text{cyl}}, \bar{\Sigma}_{\text{cyl}}]$. It follows from (2.2) and (2.11) that the parameters of an infinitely long open cylinder are related by

$$\bar{P} = 2R_{\text{cyl}}^{-3}(1 - C_0 R_{\text{cyl}}) \quad (3.12)$$

and

$$\bar{\Sigma}_{\text{cyl}} = (3 - C_0 R_{\text{cyl}})(C_0 R_{\text{cyl}} - 1)/(2R_{\text{cyl}}^2). \quad (3.13)$$

These relations were derived previously in Ref. [33] by a somewhat different argument. Eliminating R_{cyl} determines $\bar{\Sigma}_{\text{cyl}}(\bar{P}, C_0)$ and, thus, the $\bar{\Sigma}$ coordinate of the limit point. There is, however, no obvious relation between the curvature at the top of the cap $U(0)_{\text{cyl}}$ and the parameters \bar{P} and C_0 . For a discussion of the other branches, see further below.

Example (b) with $\bar{P} > 0$ and $C_0 = 1.5\bar{P}^{1/3}$ [see Fig. 2(b)]. For $C_0 > \bar{P}^{1/3}$, an additional branch (dashed) arises which connects the prolate and the spherical branch. It is important to emphasize that this second branch does not bifurcate smoothly from the spheres or the prolates. In fact, the two end points of this new branch denote shapes which consist of *two* spheres and *two* prolates, respectively. The two spheres or prolates are connected by a narrow neck. Such necks arise frequently in the shapes and involve diverging curvatures C_1 and C_2 , which however, have compensating signs. Therefore, it is possible to obtain a neck which has no energy in the limit of zero diameter, i.e., in the limit where this branch approaches either the sphere or the prolate branch. We will call such a neck an *ideal* neck. We have only found such ideal necks if the curvatures $C_1^A = C_2^A \equiv C^A$ and $C_1^B = C_2^B \equiv C^B$ of the two limiting shapes A and B adjacent to the neck fulfill the relation

$$C^A + C^B = C_0. \quad (3.14)$$

In the present case, the shapes A and B are identical and symmetric. Then this relation simplifies to

$$U(0) = C_0/2. \quad (3.15)$$

This value is indicated in Fig. 2(b) by an arrow.

Example (c) with $\bar{P} > 0$ and $C_0 = 2\bar{P}^{1/3}$ [see Fig. 2(c)]. As the spontaneous curvature C_0 is further increased, the spiral prolate branch and the additional branch which connects the sphere and the prolate branch rearrange. Moreover, additional branches arise which terminate at the branches already present. At these limit points, the shapes approach limit shapes which consist of three segments involving two ideal necks, as displayed in Fig. 2(c).

Example (d) with $\bar{P} < 0$ and $C_0 = 1.27|\bar{P}|^{1/3}$ [see Fig.

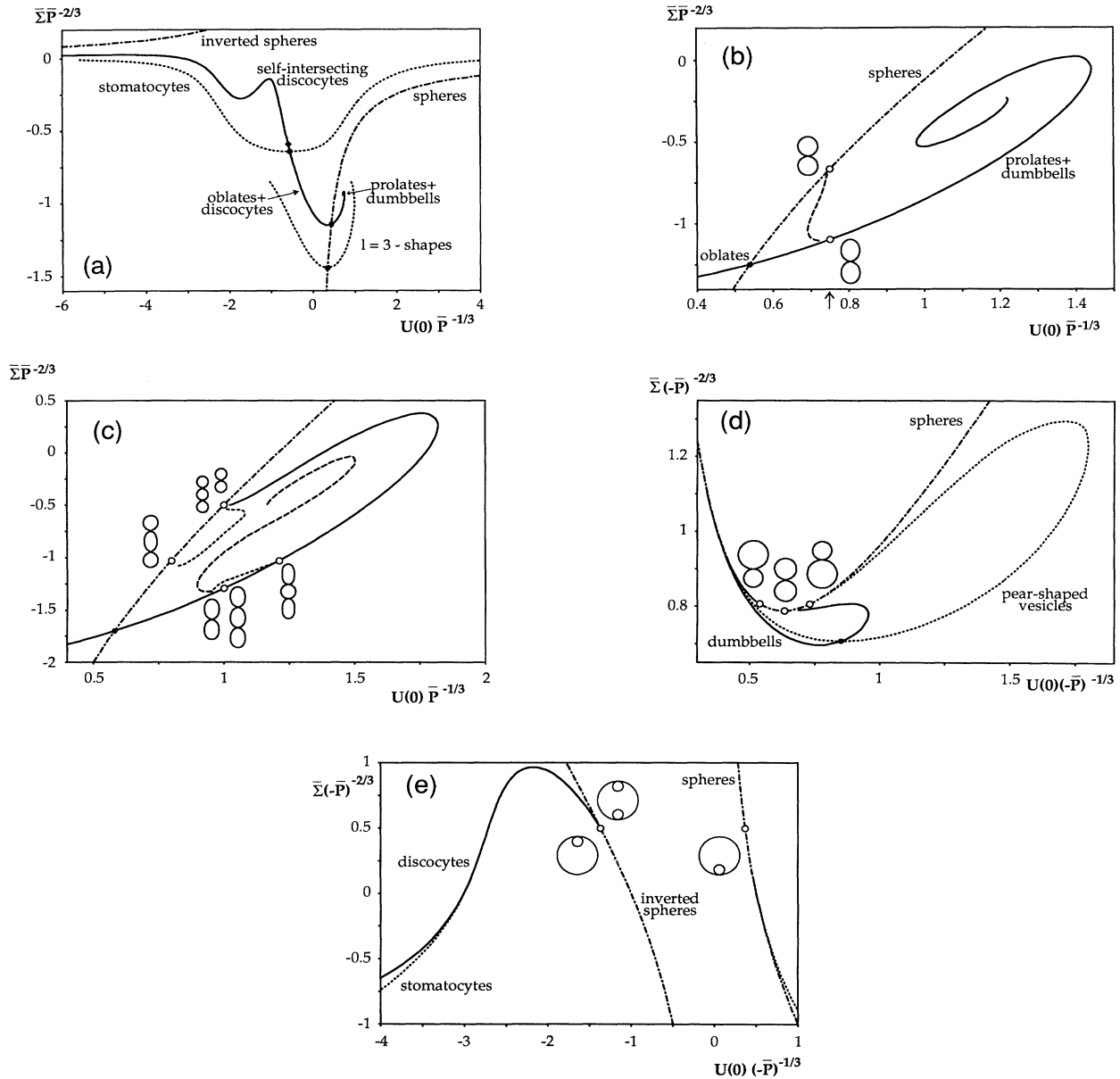


FIG. 2. Stationary shapes for fixed pressure \bar{P} and spontaneous curvature C_0 in the $(\bar{\Sigma}, U(0))$ plane, which denote the lateral tension and the curvature at the north pole, respectively. The sphere and inverted sphere branch are shown dashed-dotted. Symmetric branches are shown by solid and dashed lines, asymmetric branches by dotted lines. Bifurcations and limit points are marked with a solid and an open dot, respectively. Limit shapes are displayed. The length scale is set by $|\bar{P}|^{-1/3}$. (a) $\bar{P} > 0, C_0 = 0$. The prolate-dumbbell branch spirals to a limit point (not shown) which corresponds to a long capped cylinder. The $l=3$ branch is also displayed. The oblate-discocyte shapes are self-intersected beyond the diamond. (b) $\bar{P} > 0, C_0 = 1.5 \bar{P}^{1/3}$. A further symmetric branch (dashed) has emerged. The two loci of its limit points fulfill (3.15), as indicated by an arrow. The limit shapes at the upper and lower limit point are two spheres and two prolates, respectively. (c) $\bar{P} > 0, C_0 = 2 \bar{P}^{1/3}$. Four symmetric branches are shown. The solid line corresponds to the prolate-dumbbell branch bifurcating from the sphere branch. It approaches again the sphere branch with a limit shape given by two spheres. The long-dashed line denotes a branch which approaches the normal prolate branch with a limit shape given by two prolates and spirals to the capped cylinder. The two short-dashed lines correspond to branches which approach at the limit points shapes consisting of three segments. Additional branches without up-down symmetry occur but are not displayed. (d) $\bar{P} < 0, C_0 = 1.27 |\bar{P}|^{1/3}$. The dotted line corresponds to pear-shaped vesicles bifurcating from the prolate-dumbbell branch. The two limit points for the pear-shaped vesicles fulfill (3.16). The limit point for the prolate-dumbbell branch is given by (3.15). (e) $\bar{P} < 0, C_0 = -|\bar{P}|^{1/3}$. The dotted lines in the right and left corners denote stomatocytes which approach the limit shapes given by an inverted sphere embedded in a larger sphere. The left part seems to merge with the solid line which denotes discocytes approaching the same limit point at the sphere branch with the symmetric limit shape.

2(d)]. In this case, the ($l=2$) instability of the sphere is not present in the $[U(0), \bar{\Sigma}]$ plane. Nevertheless, prolate-dumbbell shapes are found which approach the sphere branch as $U(0)$ goes to 0 and as $U(0)$ approaches the value $C_0/2$ as given by (3.15). In the latter case, the shape approaches again the limit shape of two spheres connected by an ideal neck.

The important novel feature in case (d) is the occurrence of *pear-shaped* vesicles which break the up-down symmetry of the prolate shapes and bifurcate from this branch. This pear-shaped branch contains each shape twice since mirror shapes arise separately. Therefore, the Lagrange multiplier $\bar{\Sigma}$ acquires its extremum at the bifurcation point. For $C_0 > |2\bar{P}|^{1/3}$, which is the case considered here, these pearlike shapes approach limit shapes which consist of two spheres of different radii R_1 and R_2 again connected by an ideal neck. Both radii obey the relation (3.9) valid for spheres. It then follows from (3.14) that the end points of the pear-shaped vesicles are characterized by the relation

$$\bar{\Sigma} = C_0^2/2. \quad (3.16)$$

Now return to Fig. 2(a) for $C_0=0$ and focus on the *oblate branch* which bifurcates from the spherical branch to the other side. This branch crosses the axis $U(0)=0$. For $U(0)<0$, the shapes are biconcave discocytes, which look like red blood cells. Thus, a continuous variation leads from the oblate ellipsoids to discocytes.

Eventually, the oblate branch becomes unstable with respect to the up-down symmetry. At this point, the *stomatocyte branch* bifurcates which also contains each shape twice since mirror shapes arise separately. In the limit of large $U(0)$, the stomatocyte branch approaches the sphere branch and the inverted sphere branch, respectively. In fact, in this limit, the stomatocytes approach a shape that consists of a sphere and of an inverted sphere of equal radii which are connected by an ideal neck.

If the oblate-discocyte branch is continued beyond the bifurcation of the stomatocytes, a point is reached where the discocyte shape self-intersects. This defines the physical limit of the model although the shapes can be mathematically continued beyond this point. Then, these shapes also approach the spherical branch as $U(0)$ goes to $-\infty$. The mathematical limit shape is given by two inverted spheres embedded in a sphere with the same radius.

Example (e) with $\bar{P} < 0$ and $C_0 = -|\bar{P}|^{1/3}$ [see Fig. 2(e)]. In this case, the discocytes approach a limit shape where two inverted spheres of radius $R_1 < 0$ are embedded in a larger sphere of radius $R_2 > 0$. The end point of the discocytes approach the sphere branch for $\bar{\Sigma} = C_0^2/2$. Moreover, two identical stomatocyte branches approach a limit shape which consists of a small inverted sphere of the same radius R_1 embedded in a large sphere. Once again, these limits are given by the intersection of (3.16) with the sphere branches. It is numerically rather difficult to reach this limit point, since the branches are so close together.

The diagrams shown in Fig. 2 lead to general insight

into the structure of the branches of the stationary shapes. We now turn to the determination of the phase diagram in each of the two ensembles separately.

IV. PHASE DIAGRAM FOR THE BILAYER-COUPLING MODEL

In this section we discuss the phase diagram for the bilayer-coupling model. First, we determine the region of existence of the prolate-dumbbell, the pear-shaped, the oblate-discocyte, and the stomatocyte branches, respectively. Secondly, we compare the bending energy in regions where solutions of different branches overlap. Because of the scale invariance of the bending energy, the phase diagram depends only on two dimensionless variables v and Δa . The reduced volume v is given by

$$v \equiv \frac{V}{(4\pi/3)R_0^3}, \quad (4.1)$$

where

$$R_0 \equiv (A/4\pi)^{1/2} \quad (4.2)$$

is the radius of a sphere with the same area. The reduced area difference Δa is determined by the area difference ΔA or the integrated mean curvature M , from (2.5) and (2.6), as

$$\Delta a \equiv M/(4\pi R_0). \quad (4.3)$$

For a sphere, one has $v = \Delta a = 1$.

The phase diagram in the $(v, \Delta a)$ plane is shown in Fig. 3. It turns out that (i) the region where solutions of the oblate and stomatocyte branches exist and (ii) the region where the solutions of the prolate and pear-shaped branches exist do *not* overlap. Therefore, the phase diagram consists of two parts which we discuss separately.

As a fundamental result, we find that all shape transformations are *continuous*, i.e., the first derivative of the energy G_b with respect to v or Δa is continuous at the transformation point.

A. Prolate, dumbbell, and pear-shaped states

As shown in Fig. 3, shapes of the prolate-dumbbell branch exist in a certain region of the phase diagram which is, for $v > \sqrt{2}/2$, bounded by the lines L_1^{pro} and L_2^{pro} . In the region where these symmetric solutions exist, the line C^{pear} denotes an instability line of these shapes. They become unstable with respect to a mode which has no up-down symmetry. Between the curves C^{pear} and L^{pear} , pear-shaped vesicles exist, which always have a lower bending energy than the symmetric states for the same Δa and v (compare Fig. 4), where the functional dependence of $G_b(\Delta a)$ is given for $v=0.8$. In the region bounded by the lines C^{pear} and L_1^{pro} , the symmetric states correspond to locally *unstable* shapes. In Fig. 5 we show symmetric and asymmetric shapes for $v=0.8$.

At the transition line C^{pear} , the amplitude η of the unstable mode can be considered as an *order parameter* in a

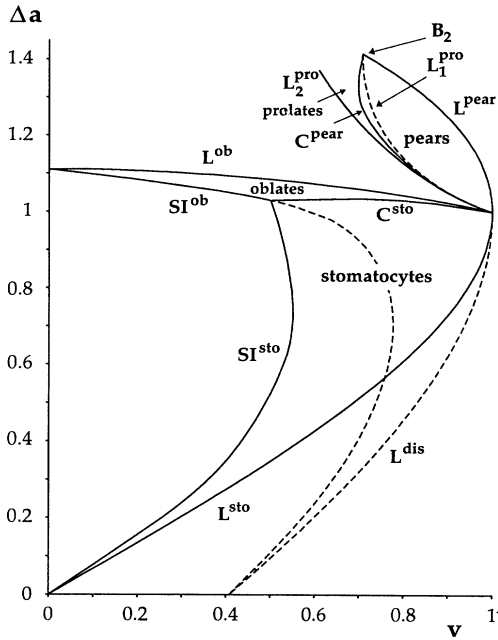


FIG. 3. Phase diagram of the bilayer-coupling model. This phase diagram shows the state of lowest energy for given Δa and v . C^{pear} denotes the line of continuous transitions between symmetric prolate-dumbbell shapes and the asymmetric pear-shaped states. Likewise, C^{sto} denotes the locus of the continuous transitions between the oblate-discocyte shapes and the stomatocytes. L^{pear} and L^{sto} are limit curves which correspond to budding and the inclusion of a spherical cavity, respectively. In the region between the prolate-dumbbell and discocyte regimes, bounded by the lines L_2^{pro} and L^{ob} , nonaxisymmetric shapes have lowest energy. The point B_2 , with $\Delta a = \sqrt{2}$ and $v = \sqrt{2}/2$, denotes the point where two spheres of equal radii are sitting on top of each other. For $\Delta a \approx \sqrt{2}$ and $v < \sqrt{2}/2$, further transitions and limit lines not yet investigated occur. The lines SI^{ob} and SI^{sto} denote lines where the two poles of the shape touch each other. The dashed lines L^{dis} , L_1^{pro} , and the continuation of SI^{ob} refer to the limit of locally unstable symmetric shapes.

Landau-type expansion. In terms of η , the energy G_b in the vicinity of the transition is given by

$$G_b = \text{const} + Q_2(v, \Delta a)\eta^2 + Q_4(v, \Delta a)\eta^4. \quad (4.4)$$

At the transition line C^{pear} , the coefficient Q_2 is zero, while Q_4 is positive.

The pear-shaped vesicles approach the line L^{pear} of limit shapes which consist of two spheres of different radii, R_1 and R_2 , connected by an ideal neck. For this shape, the integrated mean curvature defined in (2.5) is simply given by $M = 4\pi(R_1 + R_2)$. It then follows from (4.1)–(4.3) that

$$R_1 + R_2 = \Delta a R_0, \quad (4.5a)$$

$$R_1^2 + R_2^2 = R_0^2, \quad (4.5b)$$

and

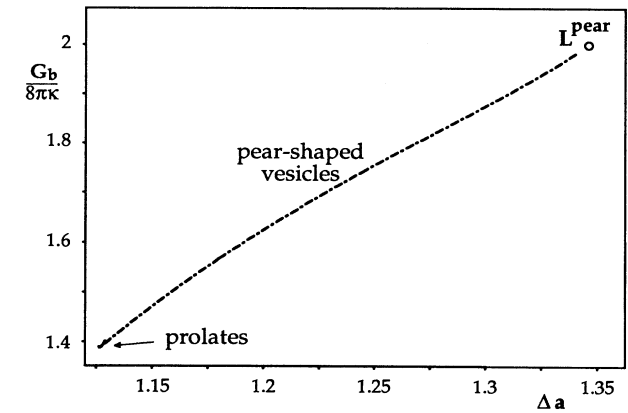
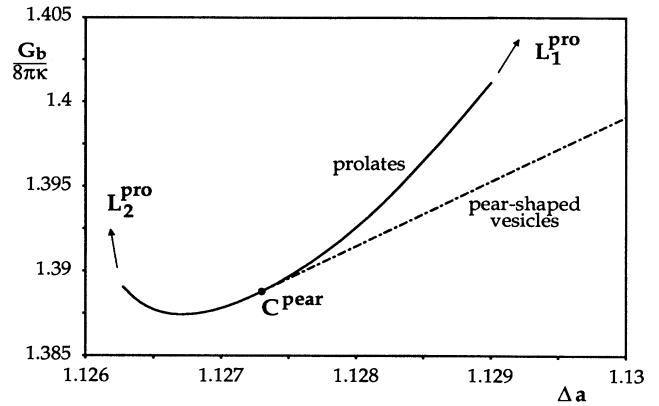


FIG. 4. Bending energy as a function of the reduced area difference for $v=0.8$. Note the different scales for Δa . C^{pear} denotes the continuous transition from symmetric (solid) to asymmetric (dashed-dotted) shapes. The points L_1^{pro} , L_2^{pro} , and L^{pear} denote limit shapes for these branches which consist of two intersecting spheres, a capped cylinder, and two spheres sitting on top of each other, respectively.

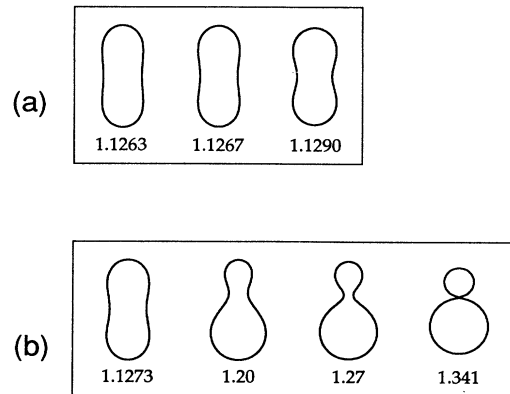


FIG. 5. Stationary shapes for $v=0.8$ and several values of Δa . (a) Symmetric shapes; the rightmost shape is locally unstable. (b) Asymmetric pear-shaped vesicles; all are locally stable.

$$R_1^3 + R_2^3 = vR_0^3. \quad (4.5c)$$

A little bit of algebra then leads to

$$vL^{\text{pear}}(\Delta a) = 1 - 3(\Delta a - 1)^2/2 - (\Delta a - 1)^3/2, \quad (4.6)$$

with $\Delta a > 1$, which describes the line L^{pear} . At L^{pear} , the bending energy G_b approaches the value $16\pi\kappa$ corresponding to two spheres.

The symmetric shapes assume simple limit shapes at the lines L_1^{pro} , L_2^{pro} , and L^{dumb} . The limit shape L_1^{pro} of the unstable part of the prolate branch is given by two intersecting spheres of the same radius. This limit shape has infinite bending energy and therefore G_b diverges as the limit is approached. This implies with (2.8) and (2.12) that $C_0 \rightarrow \infty$ and $\bar{P} \rightarrow -\infty$ at this limit. The limit shape L_2^{pro} of the stable part of the prolate branch is given by a cylinder capped with half-spheres. Such a shape has a finite bending energy. Numerically, we find that the approach to this limit shape is governed by

$$G_b(\Delta a^*) - G_b(\Delta a) \simeq (\Delta a - \Delta a^*)^\alpha$$

with $\alpha \simeq 0.2$, if Δa^* denotes the value of the limit shape.

The three curves C^{pear} , L_1^{pro} , and L^{pear} meet in the special point B_2 , with the coordinates

$$(v, \Delta a) = (\sqrt{2}/2, \sqrt{2}), \quad (4.7)$$

where two spheres of equal radii are connected by an ideal neck.

For $v < \sqrt{2}/2$, the phase diagram becomes more complex since an increasing number of limit shapes becomes available. These limit shapes consist of several spheres (with at most two different radii) connected by ideal necks which obey (3.14) or ellipses connected by ideal necks with spheres [35]. We have not yet attempted to investigate this region of the phase diagram systematically.

B. Oblate, discocyte, and stomatocyte shapes

Since this part of the phase diagram has already been described by Svetina and Zeks [25], we give only a short summary for completeness. Oblate and discocyte shapes exist in the region bounded by the curves L^{ob} , L^{dis} , and SI^{ob} (see Fig. 3). The limit shapes at L^{ob} consist of two spherical caps. At L^{dis} , the limit shapes are given by a sphere which encloses two smaller spheres. The curve SI^{ob} denotes shapes where the north and south poles touch each other, i.e., the shapes begin to self-intersect. For even smaller volume beyond SI^{ob} , self-intersection of the bilayer must be taken into account in order to prevent this self-intersection [36]. If one allows for topological changes of the vesicle shape, this line of the phase diagram will be related to formation of a hole through the vesicle and, thus, to the occurrence of toroidal vesicles [37].

At the line C^{sto} , the oblate and discocyte shapes become unstable with respect to a deformation that breaks the up-down symmetry and undergo a shape transformation towards the stomatocytes. Therefore, the symmetric states are locally unstable in a region bounded by the

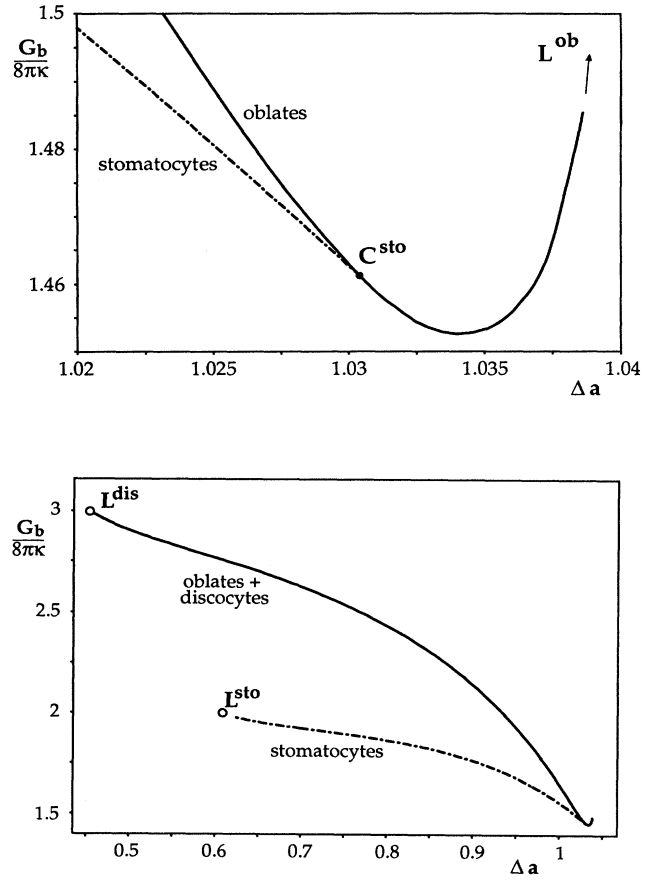


FIG. 6. Bending energy as a function of the reduced area difference for $v=0.8$. Note the different scales for Δa . C^{sto} denotes the continuous transition from symmetric (solid) to asymmetric (dashed-dotted) shapes. The points L^{ob} , L^{dis} , and L^{sto} denote limit shapes for these branches, which are given by two opposing spherical caps, two inverted spheres embedded in a larger one, and the inclusion of a spherical cavity in a larger sphere, respectively.

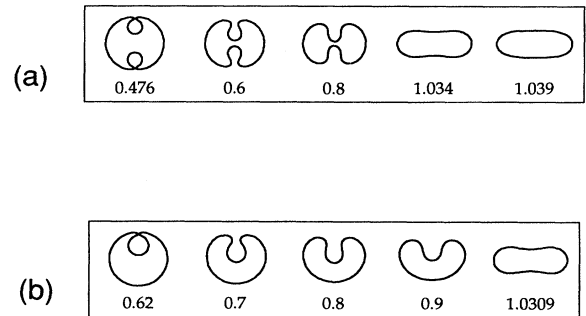


FIG. 7. Stationary shapes for $v=0.8$ and several values of Δa . (a) Symmetric shapes; the three leftmost shapes are locally unstable. (b) Stomatocytes; all shapes are locally stable.

lines C^{sto} , L^{dis} , and SI^{ob} (see Fig. 3). This shape transformation can again be understood by a Landau-type expansion, as in (4.4).

The stomatocytes exist in a region bounded by the lines C^{sto} , L^{sto} , and SI^{sto} , where they always have lower energy than the symmetric shapes. At L^{sto} , the limiting shapes consist of a sphere that encloses a smaller sphere. Both spheres are connected by an ideal neck. The locus L^{sto} is given by (4.6) with $0 < \Delta a < 1$. In Fig. 6 we show the bending energy and in Fig. 7 the shapes of the two branches for $v=0.8$. The bending energy diverges at L^{ob} and remains finite at L^{dis} and L^{sto} .

C. Further branches of solutions

So far, we have discussed prolate and oblate shapes arising from the ($l=2$) bifurcation of the sphere and the symmetry-breaking pearlike and stomatocyte shapes. In the phase diagram of Fig. 3 the gap between the limit shapes L_2^{pro} and L^{ob} implies that this region contains no axisymmetry ($l=2$) shapes. On the other hand, this region contains shapes that derive from the ($l \geq 3$) bifurcation of the sphere. Peterson [34] has found, however, that these shapes are locally unstable with respect to elliptical deformations in the spherical limit, i.e., as v goes to 1. His argument is based on the general expression for the second variation of the bending energy in this limit. It holds irrespectively whether the spontaneous-curvature model or the bilayer-coupling model is considered. This implies that if the gap contains locally stable shapes at all, these must be *nonaxisymmetric* ($l=2$) shapes. How far this region of stable nonaxisymmetric shapes extends into the prolate and oblate region cannot be answered without a more detailed analysis.

Finally, it is remarkable that the boundary lines L_1^{pro} , L_2^{pro} , and L^{ob} approach the sphere point $(v, \Delta a) = (1, 1)$ with the same derivative

$$\left. \frac{d\Delta a}{dv} \right|_{v=1} = -\frac{1}{3}. \quad (4.8)$$

As proven in Appendix C, this relation holds even more generally for any curve $(v(t), \Delta a(t))$ of smooth shapes which approach the sphere, i.e., which can be parametrized as in (3.10) where $a_{l,m}(0) = 0$.

V. PHASE DIAGRAM FOR THE SPONTANEOUS-CURVATURE MODEL

For the spontaneous-curvature model, the phase diagram is determined by the solution of the shape equation which has the lowest bending energy F_b for a given area A and volume V . Because the bending energy is scale invariant, this phase diagram again depends only on two dimensionless parameters, which are the reduced volume $v \equiv V / [(4\pi/3)R_0^3]$ as defined by (4.1) and the reduced spontaneous curvature of c_0 as given by

$$c_0 \equiv C_0 R_0. \quad (5.1)$$

Since the branches have significantly more overlap in this model, most transitions are *discontinuous*, i.e., the first

derivative of the energy F_b is discontinuous at the transition point.

A. Phase diagram for zero spontaneous curvature

This case is certainly the minimal model for vesicle shapes and deserves a special presentation. In Fig. 8 we show the bending energy F_b as a function of the reduced volume v for the prolate-dumbbell, oblate-discocyte, and stomatocyte branches. The pear-shaped vesicles do not exist for this choice $c_0 = 0$.

The prolate-dumbbell branch exists for all $0 < v \leq 1$. With decreasing reduced volume v , the shapes along this branch vary smoothly from a prolate ellipsoid via dumbbell-like shapes to a long and narrow capped cylinder.

For $v \lesssim 1$, the shapes of the oblate-discocyte branch correspond to oblate ellipsoids. With decreasing v , these shapes become discocyte and finally self-intersect for $v = v_{SI}^{\text{ob}} \simeq 0.50$.

For $v = v_C^{\text{sto}} \simeq 0.51$, the stomatocyte branch bifurcates from the oblate branch. It reaches the maximal volume at $v = v_M^{\text{sto}} \simeq 0.66$. The lower part of this stomatocyte branch finally approaches a limit shape for small v , where an inverted sphere is connected by an ideal neck with a sphere of the same radius as required by (3.14) for $C_0 = 0$. Thus the volume vanishes and the energy goes to $16\pi\kappa$.

The form of the energy F_b as shown in Fig. 8 for the oblate-discocyte and the stomatocyte branches can again be understood in terms of a Landau-type expansion for the order parameter η which represents the amplitude of the unstable mode. As before, this mode breaks the up-down symmetry of the oblate-discocyte shapes. However, in this case, one has to include a six-order term Q_6 , which leads to

$$F_b = \text{const} + Q_2(v, c_0)\eta^2 + Q_4(v, c_0)\eta^4 + Q_6(v, c_0)\eta^6, \quad (5.2)$$

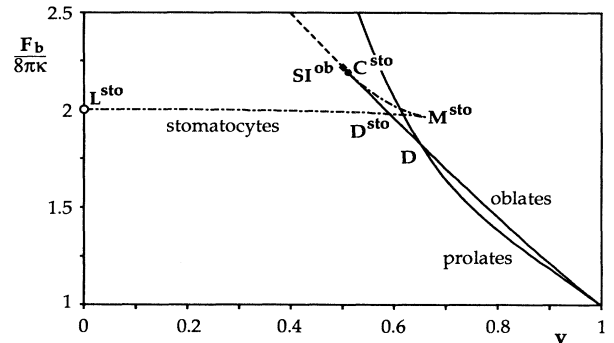


FIG. 8. Bending energy for $c_0 = 0$ as a function of the reduced volume v . Three branches are displayed: the prolate, the oblate, and the stomatocyte branches. The latter bifurcates from the oblate branch. Its upper part between C^{sto} and M^{sto} corresponds to locally unstable shapes. Its lower part between L^{sto} and M^{sto} corresponds to locally stable shapes. The oblate branch beyond SI^{ob} corresponds to self-intersected states.

with $c_0=0$.

For $v < v_C^{\text{sto}}$, the coefficients Q_2 and Q_4 are negative. At C^{sto} , Q_2 changes sign. For $v_C^{\text{sto}} < v < v_M^{\text{sto}}$, the function F_b has three local minima and two local maxima. The minima with $\eta \neq 0$ correspond to the lower stomatocyte branch which is, thus, locally stable. The minimum with $\eta = 0$ describes the symmetric oblate-discocyte branch. The local maxima correspond to unstable stomatocytes. At M^{sto} , the local minima with $\eta \neq 0$ merge with the local maxima and disappear for $v > v_M^{\text{sto}}$. In this range, only one local minimum survives.

Comparing the bending energy of the three branches—the prolate-dumbbell, the oblate-discocyte, and the stomatocyte branches—one finds that for $0 < v < v_D^{\text{sto}} \approx 0.59$, the stomatocytes have the lowest energy, while for $v_D^{\text{sto}} < v < v_D \approx 0.65$, the oblate shapes have lowest energy. Since the oblate shapes are discocytes in this regime, no spontaneous curvature is necessary in order to stabilize biconcave shapes, as previously observed by Svetina and Zeks [25]. For $v_D^{\text{sto}} < v < 1$, finally, the prolate shapes correspond to the ground state. In Fig. 9 we show the shapes of lowest bending energy for several values of v . Discontinuous transitions separate the three regimes.

It is worthwhile to observe also that the energy barrier ΔF_b between the oblate and the stomatocyte shapes can be derived from Fig. 8. It is given by the energy difference between the oblate branch and the upper part of the stomatocyte branch which is the saddle point along a path of axisymmetric solutions connecting the two locally stable shapes. We find $\Delta F_b \approx 1.3\kappa$ for $v = v_D^{\text{sto}}$, i.e., at the discontinuous transition. This is typically much more than the thermal energy. Therefore, one expects hysteresis, i.e., the oblate-discocyte shapes can be extended into the “metastable” region with $v < v_D^{\text{sto}}$. The transition will then take place when the energy difference ΔF_b becomes comparable to T . Note that for the transition between the prolate and the oblate branches the activation energy cannot be read off from the energy diagram of Fig. 8, because a path connecting the prolate and the oblate branches at constant v involves nonaxisymmetric shapes.

B. Complete phase diagram

We describe in this subsection the phase diagram for $C_0 \neq 0$ as displayed in Fig. 10. The derivation of these re-

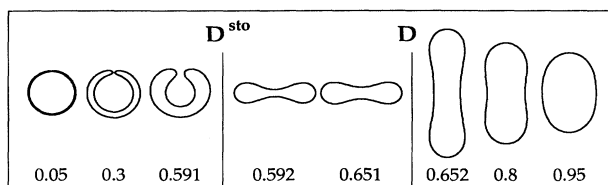


FIG. 9. Shapes for $c_0=0$ and several values of v . D and D^{sto} denote the discontinuous prolate-oblate and oblate-stomatocyte transitions, respectively. All shapes have the same area.

sults is sketched in Appendix D.

The right half of the phase diagram is divided into two parts by the line D , which denotes a discontinuous transition between the prolate-dumbbell and the oblate-discocyte branches. Above D , the prolate-dumbbell shapes have lower bending energy than the oblate-discocyte ones. As v goes to 1, it has already been derived analytically that this phase boundary approaches the critical value $c_0 = -\frac{6}{5}$ [27]. For $c_0=0$, this phase boundary is at $v_D \approx 0.65$.

For $c_0^{(2)} < c_0 \leq c_0^{(3)}$, with $c_0^{(2)} \approx 2.066$ and $c_0^{(3)} \approx 2.08$, a discontinuous transition D^{pro} between two different prolate-dumbbell shapes occurs. This line terminates in a critical point.

For $c_0^{(3)} < c_0 < 2\sqrt{2}$, the pear-shaped vesicles have lowest energy in the region which is bounded by the lines D^{pear} and C^{pear} . While the line D^{pear} denotes a line of discontinuous transitions from symmetric to pear-shaped states (and $D^{*\text{pear}}$ is an approximation to this transition as discussed in Appendix E), the line C^{pear} corresponds to a continuous transition between these states. In order to illustrate these transitions, we show in Fig. 11 the functional dependence of the bending energy $F_b(v)$ and in Fig. 12 the corresponding shapes for $c_0=2.4$. The energy diagram shows that the pear-shaped vesicles and the symmetric ones can, of course, be extended beyond the discontinuous transition D^{pear} . This region of metastability is briefly discussed in Appendix D.

For $c_0 > 2\sqrt{2}$, budding can occur, as illustrated in Figs.

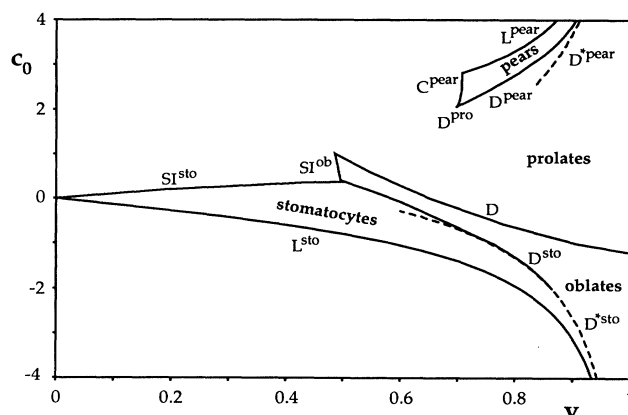


FIG. 10. Phase diagram of the spontaneous-curvature model. This phase diagram shows the shape of lowest bending energy for a given scaled spontaneous curvature c_0 and reduced volume v . The regions where the prolate-dumbbells, pears, oblate-discocytes, and stomatocytes have lowest energy are separated by transitions. The line C^{pear} denotes a continuous transition. All other transitions are discontinuous. The dashed lines $D^{*\text{pear}}$ and $D^{*\text{sto}}$ denote approximations to the discontinuous transitions as derived in Appendix E. The line L^{pear} denotes where budding occurs. The line L^{sto} corresponds to the inclusion of a spherical cavity. Beyond the lines SI^{ob} and SI^{sto} , self-intersected states occur. For $c_0 > 2\sqrt{2}$, $v < \sqrt{2}/2$, the phase diagram is not yet known.

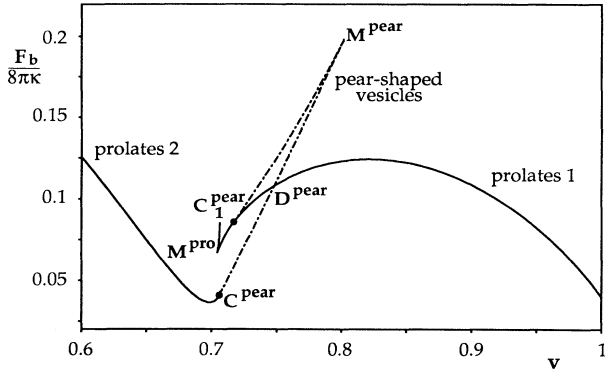


FIG. 11. Bending energy for $c_0=2.4$ as a function of the reduced volume v . Two different symmetric branches, prolate-1 and prolate-2, are connected by an asymmetric pear-shaped branch which bifurcates at C^{pear} and C_1^{pear} from the symmetric branches. The upper part of this pear-shaped state corresponds to locally unstable shapes. The prolate-1 branch attains minimal volume at M^{pro} . The energy along its upper part then presumably diverges. The prolate-2 branch ends up for $v=\sqrt{2}/2$ in the limit shape where two spheres of equal radii are connected by an ideal neck. This short continuation of the prolate-2 branch beyond the bifurcation C^{pear} is not visible on this scale.

13 and 14 where the functional dependence of $F_b(v)$ for $c_0=3$ and stationary shapes, respectively, are displayed. The pear-shaped vesicles approach a limit shape at L^{pear} , where two spheres of radii R_1 and R_2 are connected by an ideal neck. The relations (3.14), with $C^A \equiv R_1^{-1}$ and $C^B \equiv R_2^{-1}$, and (4.5b) lead to

$$C_0^{\text{pear}} = 1/R_1 + (R_0^2 - R_1^2)^{-1/2}. \quad (5.3)$$

This equation determines the required spontaneous curvature for budding of a small vesicle of radius R_1 . For small R_1 , we have $C_0^{\text{pear}} \approx 1/R_1$. Equations (5.3) and (4.5c) lead after a little bit of algebra to the location of the line L^{pear} as given by

$$v_{L^{\text{pear}}}(c_0) = -2c_0^{-3} + (1 - 2c_0^{-2})\sqrt{1 + c_0^{-2}}. \quad (5.4)$$

The line L^{pear} starts at the point B_2 , with coordinates $(c_0, v) = (2\sqrt{2}, \sqrt{2}/2)$, where two spheres of equal radii

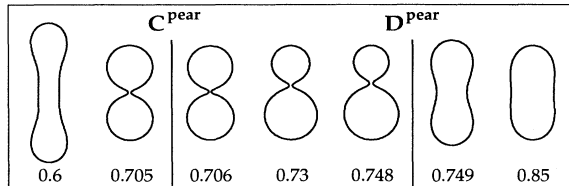


FIG. 12. Shapes along the "reentrant" trajectory for $c_0=2.4$ and several values of v . D^{pear} and C^{pear} denote a discontinuous and a continuous transition, respectively.

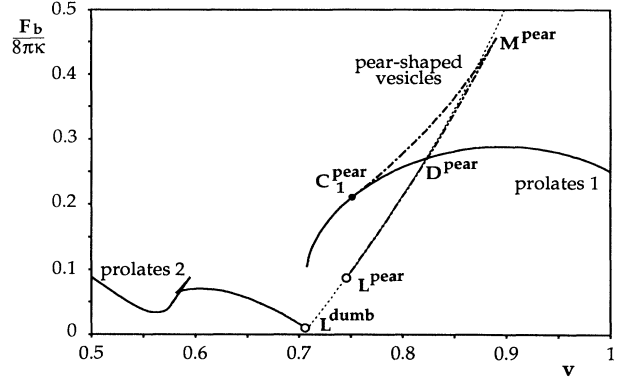


FIG. 13. Bending energy for $c_0=3$ as a function of the reduced volume v . The two different symmetric branches, prolate-1 and prolate-2, are no longer connected by the asymmetric pear-shaped branch. The latter branch bifurcates at C_1^{pear} , attains a maximal volume at M^{pear} , and ends up in a limit shape L^{pear} , where two spheres of different radii are connected by an ideal neck. The prolate-2 branch starts in the (unstable) limit shape L^{dumb} where two prolates are connected with an ideal neck. Along this branch, at least two instabilities with respect to the up-down symmetry occur which are not visible on this scale. An additional "wing" emerges for $v \approx 0.58$. The dotted line denotes an approximation to the pear-shaped states, as discussed in Appendix E.

are connected by an ideal neck. For $c_0 \geq 2\sqrt{2}$ and $v \leq \sqrt{2}/2$, further instabilities of the symmetric shapes occur. Again, we have not attempted a classification of the shape transitions in this region.

We now turn to the lower part of the phase diagram shown in Fig. 10. The oblate-discocyte shapes have lowest bending energy in the region bounded by the lines D , SI^{ob} , and D^{sto} . Beyond the line SI^{ob} , the discocyte shapes self-intersect and must be excluded physically. This is also the physical limit of the discontinuous prolate-oblate transition D . The line D^{sto} denotes a discontinuous transition between the oblate-discocyte shapes and the stomatocytes, while D^{sto} is an approxi-

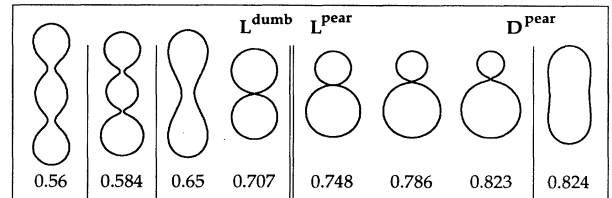


FIG. 14. Stationary shapes for $c_0=3$ and several values of v . D^{pear} denotes the discontinuous transition between the prolate-dumbbell and the pear-shaped states. The latter terminate in the limit shape L^{pear} . The prolate-2 branch starts at the (unstable) limit shape L^{dumb} . An asymmetric shape is shown for $v=0.584$. These asymmetric shapes become symmetric again with decreasing volume as displayed for $v=0.56$.

mation to this transition, as discussed in Appendix E.

It is interesting to note that the continuation of the oblate-stomatocyte transition into the region of self-intersected states leads to a tricritical point where both coefficients Q_2 and Q_4 in the Landau-type expansion (5.2) vanish. The locus of this point can be read off from Fig. 18(a) given below.

The region where the stomatocytes have lowest bending energy is furthermore bounded by the line SI^{sto} which denotes self-intersection of the stomatocytes, and the line L^{sto} . Along L^{sto} , one has limit shapes which consist of an inverted sphere of radius $R_1 < 0$ connected with an ideal neck to a sphere with radius $R_2 > 0$. The locus of the line L^{sto} is again given by the right-hand side of (5.4) but with $c_0 < 0$.

The boundaries in the region of the phase diagram determined so far are given by the lines L^{pear} , SI^{ob} , SI^{sto} , and L^{sto} , where two parts of the membrane come into close contact. In order to continue the phase diagram beyond these lines, additional interactions such as the van der Waals interaction or the repulsion arising from hydration forces must be taken into account.

VI. TRAJECTORIES IN THE PHASE DIAGRAM

In a typical experiment, the shape of a vesicle is studied by light microscopy. More precisely, one observes a one-dimensional contour of the two-dimensional vesicle surface. This contour allows a determination of the area A and the volume V and thus of the reduced volume v of the vesicle provided (i) the vesicle is indeed axisymmetric with its axis parallel to the image plane and (ii) fluctuations of the vesicle contour are not too strong. For a freely floating vesicle, condition (i) will only be fulfilled for a relatively small fraction of the observation time. Condition (ii) depends crucially on the ratio T/κ which sets the scale for fluctuations. For the typical values $\kappa \simeq 10^{-19}$ J, $T \simeq 4 \times 10^{-21}$ J and $T/\kappa \simeq 0.04$, experiments yield a well-defined contour. In order to determine Δa , one needs the value of the integrated mean curvature which may also be inferred from the contour via (2.5), (4.2), and (4.3).

Therefore, the relevant parameters v and Δa for the bilayer-coupling model are, at least in principle, deducible from the observed contour. In contrast, we are not aware of any method by which one can directly control or measure the spontaneous curvature C_0 .

Transformations of different vesicle shapes are experimentally induced by a change in temperature or the osmotic conditions. Therefore, we will now discuss the corresponding trajectories in the phase diagrams of the bilayer-coupling and the spontaneous-curvature models.

A. Temperature trajectories in the bilayer-coupling model

An increase in temperature results in thermal expansion of the two monolayers and the enclosed water. We admit different thermal expansivities α^{in} and α^{ex} of both monolayers as given by [31]

$$\alpha^{\text{in}} \equiv \frac{1}{A^{\text{in}}} \frac{dA^{\text{in}}}{dT} \equiv \alpha \quad (6.1a)$$

and

$$\alpha^{\text{ex}} \equiv \frac{1}{A^{\text{ex}}} \frac{dA^{\text{ex}}}{dT} \equiv (1 + \gamma)\alpha, \quad (6.1b)$$

which defines γ . The expansivity of the reference surface can be written as

$$\frac{1}{A} \frac{dA}{dT} \equiv (1 + \bar{\gamma})\alpha, \quad (6.2)$$

where $\bar{\gamma}$ is of the order of γ and can be expressed by the parameters of the two monolayers (see Appendix A).

We moreover allow the separation D of the two monolayers to become temperature dependent as given by

$$\frac{1}{D} \frac{dD}{dT} \equiv \alpha_D. \quad (6.3)$$

The expansivity of the enclosed water is written as

$$\frac{1}{V} \frac{dV}{dT} \equiv \alpha_V. \quad (6.4)$$

With (4.1), (4.3), and (2.6), we obtain for the temperature dependence of the reduced volume v and area difference Δa the expressions

$$\frac{dv}{dT} = v[\alpha_V - (1 + \bar{\gamma})3\alpha/2] \quad (6.5)$$

and

$$\begin{aligned} \frac{d\Delta a}{dT} = & a^{\text{ex}}[\alpha(1 + \gamma) - \alpha_D - \alpha(1 + \bar{\gamma})/2] \\ & - a^{\text{in}}[\alpha - \alpha_D - \alpha(1 + \bar{\gamma})/2], \end{aligned} \quad (6.6)$$

with

$$a^{\text{ex}} \equiv \frac{A^{\text{ex}}}{4D(\pi A)^{1/2}} \quad (6.7a)$$

and

$$a^{\text{in}} \equiv \frac{A^{\text{in}}}{4D(\pi A)^{1/2}}. \quad (6.7b)$$

The T dependence of a^{ex} and a^{in} directly follows from (6.1) to (6.3). If we assume that all coefficients of expansivity are temperature independent, the differential equations for v and Δa can be integrated and yield

$$v(T) = v(T_0) \exp\{[\alpha_V - (1 + \bar{\gamma})3\alpha/2](T - T_0)\} \quad (6.8)$$

and

$$\begin{aligned} \Delta a(T) = & e^{[\alpha(1 + \bar{\gamma})/2 - \alpha_D](T - T_0)} \\ & \times [a^{\text{ex}}(T_0)e^{\gamma\alpha(T - T_0)} - a^{\text{in}}(T_0)]. \end{aligned} \quad (6.9)$$

Eliminating $T - T_0$ in both equations, one finds for a temperature trajectory the expression

$$\Delta a = (v_0/v)^r \{\Delta a_0 + b[(v_0/v)^q - 1]\}, \quad (6.10)$$

where $\Delta a_0 \equiv \Delta a(T_0)$ and $v_0 \equiv v(T_0)$. The exponents r and q are of the order unity and given by

$$r = [\alpha(1 + \bar{\gamma})/2 - \alpha_D] / [(1 + \bar{\gamma})3\alpha/2 - \alpha_V] \quad (6.11)$$

and

$$q = \alpha / [(1 + \bar{\gamma})3\alpha/2 - \alpha_V]. \quad (6.12)$$

The dimensionless coefficient b is given by

$$b \equiv a^{\text{ex}}(T_0) = A^{\text{ex}}(T_0) / \{4D(T_0)[\pi A(T_0)]^{1/2}\}. \quad (6.13)$$

The volume expansivity of water is considerably smaller than the area expansivity α . Typical values are $\alpha \approx 6 \times 10^{-3}/K$ and $\alpha_V \approx 3 \times 10^{-4}/K$ [12]. Therefore, one may neglect α_V in r and q .

First, consider the case without asymmetry, i.e., $\gamma = \bar{\gamma} = 0$, which leads to the simple expression

$$\Delta a = \Delta a_0 (v_0/v)^r. \quad (6.14)$$

Two limiting cases can be considered: (i) If the monolayer separation D does not change with temperature, one has $\alpha_D = 0$ which leads to $r = \frac{1}{3}$. (ii) If D decreases with temperature in such a way that the bilayer volume as given by $\sim AD$ remains temperature independent, i.e., $\alpha_D = -\alpha$, one has $r = 1$.

Second, consider the influence of the asymmetry parameter γ . The dimensionless coefficient b in (6.13) is typically of order 10^3 , as can be estimated from the values $A^{\text{in}} \approx A^{\text{ex}} \approx A \approx 1000 \mu\text{m}^2$ and $D \approx 5 \text{ nm}$. Thus, an asymmetry γ of the order 10^{-3} already has a considerable influence [31]. This is demonstrated in Fig. 15, where trajectories for several values of γ are shown in the phase diagram for $\alpha_D = -\alpha_V$ and $\bar{\gamma} = \gamma/2$ and the same

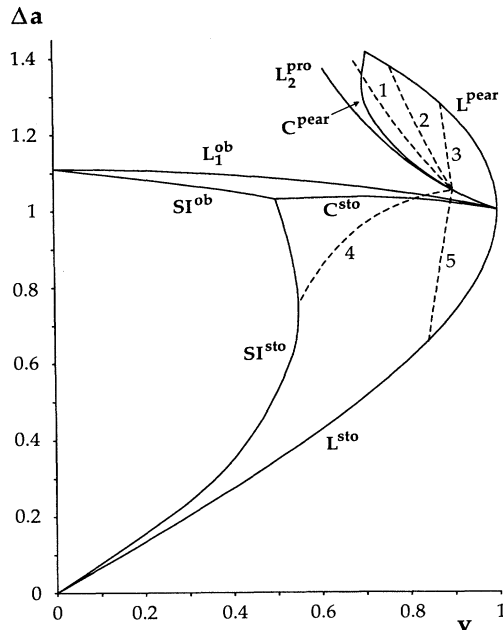


FIG. 15. Temperature trajectories in the phase diagram for the bilayer-coupling model as given by (6.10)–(6.13) for several values of the asymmetry parameter γ . (1) $\gamma = 0$, (2) $\gamma = 0.001$, (3) $\gamma = 0.01$, (4) $\gamma = -0.018$, and (5) $\gamma = -0.01$ and the same initial value $(\Delta a_0, v_0) = (0.9, 1.0504)$, which corresponds to a prolate ellipsoid with $c_0 = 0$. The other parameters were given by $b = 1000$, $\bar{\gamma} = \gamma/2$, $\alpha_D = -\alpha$, and $\alpha_V = 0$.

initial value $(v_0, \Delta a_0) = (0.9, 1.05)$ which corresponds to a prolate ellipsoid. These trajectories lead to different sequences of shape transformation depending on the value of γ :

(i) *Reentrant trajectory.* For small $|\gamma| \lesssim 10^{-4}$, the vesicle first enters the pear-shaped region but eventually becomes symmetric again. Both transitions are continuous.

(ii) *Budding trajectory.* For $\gamma \gtrsim 10^{-3}$, the trajectory enters the pear-shaped region and finally attains the line L^{pear} where a small vesicle has been budded off. The size of this vesicle depends on γ . The larger γ is, the smaller the expelled vesicle.

(iii) *Prolate-oblate transition.* For $\gamma \lesssim -10^{-3}$ the vesicle leaves the prolate region. As discussed in Sec. IV C, we expect that nonaxisymmetric shapes have lowest energy in this case. For sufficiently large $|\gamma|$, this trajectory will enter the oblate region, where we expect that it becomes axisymmetric again. If the trajectory is continued it may attain the following.

(iv) *Oblate-stomatocyte transition.* A trajectory starting in the oblate region can cross the phase boundary C^{sto} and will then (i) meet the line SI^{sto} where the two poles come into contact or (ii) will end up, for larger $|\gamma|$ with $\gamma < 0$, at the line of limit shapes L^{sto} where a small cavity is enclosed. The larger $|\gamma|$ is, the smaller the cavity.

The sequences (i), (ii), and (iv) have indeed been observed recently and compared with the theoretical predictions. These results were reported in our previous letter [31]. The parametrization of the trajectories used there is a special case of (6.10) to (6.13) with the following simplifying assumptions: (i) The inner monolayer is taken as the reference surface which leads to $\bar{\gamma} = 0$ and (ii) we assumed that the volume of the bilayer is temperature independent, i.e., $\alpha_D = -\alpha$. One then has the exponents $r = 1$ and $q = \frac{2}{3}$.

Finally, consider a temperature trajectory as in (6.10) which starts from the sphere with $(v, \Delta a) = (1.0, 1.0)$. Close to the sphere, the shapes of lowest energy exhibit a small bud. In the spherical limit, the size of this bud goes to zero, but its energy approaches a nonzero value smaller than $8\pi\kappa$. Indeed, any path $\Delta a(v)$ in the phase diagram which does not contain such a bud in this limit, i.e., which corresponds to shapes parametrized by spherical harmonics as in (3.10), approaches the sphere with $d\Delta a(v)/dv = -\frac{1}{3}$, as in (4.8). However, the shapes with the bud can only be applied to real vesicles as long as the size of this bud is large compared to the size of the shape fluctuations, which are of the order of $(T/\kappa)^{1/2}R_0$. On the other hand, it can be derived from (4.5) and (4.6) that the size of the bud goes like $(1-v)^{1/2}R_0$.

B. Temperature trajectories in the spontaneous-curvature model

A discussion of the trajectories in the spontaneous-curvature model is difficult since the temperature dependence of the spontaneous curvature is not obvious. For the special case, $c_0 = 0$, however, it is sufficient to use the temperature dependence of $v(T)$ as given by (6.8) and to recall the results discussed in Sec. V A. A temperature trajectory leads to a discontinuous transition at

$v(T) \approx 0.65$ between a dumbbell and a discocyte state which involves presumably nonaxisymmetric shapes. A further discontinuous transition at $v \approx 0.59$ then leads from discocytes to stomatocytes. If the discocytes are continued into the metastable region, the value $v = v_C^{\text{sto}} \approx 0.51$ gives a lower bound for this transition to set in since the discocytes are locally unstable for $v < v_C^{\text{sto}}$. Note that starting from the sphere at $v = 1$, a temperature difference $T - T_0 \approx 60$ K is required in order to reach the transition at $v_D^{\text{sto}} \approx 0.59$ for the typical value $\alpha \approx 6 \times 10^{-3}$ / K [12].

For $c_0(T) \neq 0$, several sequences of shape transformation can be obtained. For simplicity, we again assume that $c_0(T) = c_0$ is temperature independent. Then a temperature trajectory is parallel to the v axis of the phase diagram shown in Fig. 10. Sequences related to those discussed above for the bilayer-coupling model are characterized in the spontaneous-curvature model by the following features:

(i) *Reentrant trajectory.* Such a trajectory occurs for $c_0^{(3)} \leq c_0 \leq 2\sqrt{2}$, with $c_0^{(3)} \approx 2.08$. The symmetric prolate vesicle first undergoes a *discontinuous* transition to the asymmetric pear-shaped state. A further increase in temperature then leads to a *continuous* transition back to a symmetric shape (compare Figs. 11 and 12 for the energy and the shapes for $c_0 = 2.4$). The two main differences of this type of trajectory compared to the bilayer-coupling model are (i) the first discontinuous transition which should lead to hysteresis and (ii) the narrow neck when the vesicles become symmetric again.

(ii) *Budding trajectory.* Such a trajectory requires $c_0 > 2\sqrt{2}$. A discontinuous transition leads from symmetric prolate or dumbbell shapes to asymmetric pear-shaped states (compare Figs. 13 and 14 for $c_0 = 3$). The larger c_0 is, the smaller the expelled vesicle as expressed by the relation (5.3). The main difference compared to the bilayer-coupling model is once again the character of the transition. Moreover, pear shapes with a slight asymmetry are locally unstable in the spontaneous-curvature model and, thus, do not occur as equilibrium shapes as they do in the bilayer-coupling model.

(iii) *Prolate-oblate transition.* This transition requires $1 \gtrsim c_0 > -1.2$. For the axisymmetric shapes considered here, the transition is discontinuous and the shape transformation might involve nonaxisymmetric shapes. A detailed analysis of this process and the corresponding energy barrier has not been attempted so far.

(iv) *Oblate-stomatocyte transition.* This transition is also discontinuous and requires $c_0 \lesssim 0.4$. For $c_0 < 0$, the vesicle attains a limit shape at L^{sto} where a small cavity is enclosed with increasing temperature. As $|c_0|$ is increased, the size of the cavity becomes smaller and the temperature difference which is required in order to reach this limit shape also decreases.

C. Osmotically induced shape transformations

Shape transformations can also be induced by a change in the osmotic conditions. Let us assume (i) that a vesicle with volume V contains n moles of a solute like sugar which cannot permeate through the membrane and (ii)

the concentration c in moles per volume of the solute in the exterior solution can be controlled. Then an osmotic pressure Π is present, which is given by

$$\Pi = RT(n/V - c), \quad (6.15)$$

where R is the gas constant, assuming that the solution is ideal. The vesicle responds with permeation of solvent through the membrane which leads to a change in volume and thus in the interior concentration of solute n/V . The equilibrium condition is given by

$$-\frac{\partial G_b}{\partial V} = \Pi(V) \quad (6.16a)$$

or

$$-\frac{\partial F_b}{\partial V} = \Pi(V) \quad (6.16b)$$

for the two models, respectively. The left-hand side of these relations is of the order of $8\pi\kappa/V \approx 6 \times 10^{-4}$ J/m³, for $\kappa = 10^{-19}$ J and $V = \frac{4}{3}\pi(10 \mu\text{m})^3$. It then follows from (6.15) with $RT \approx 2.5 \times 10^3$ J/mol, for $T \approx 300$ K, that only extremely small concentration differences of the order 10^{-7} mol/m³ can be balanced by the curvature term. Therefore, the vesicle must adjust its volume close to the value $\bar{V} \equiv n/c$ in order to achieve this balance. In this way, a change in the solute concentration c leads to a variation of the volume v [16].

If the solute does not couple to the membrane, i.e., if ΔA or C_0 do not change with c , a variation of c will lead to *horizontal* trajectories parallel to the v axis in the phase diagrams shown in Figs. 3 and 10. Inspection of Fig. 3 shows, that thus in the bilayer-coupling model, neither budding nor the inclusion of a cavity is accessible by increasing the solute concentration. In contrast, in the spontaneous-curvature model, trajectories parallel to the v axis can exhibit both phenomena (compare Fig. 10). Therefore, if budding were observed by increasing the solute concentration, one would have to conclude (i) that the spontaneous-curvature model is appropriate for this system or (ii) that the membrane properties have changed by adding the solute which may also lead to an anomalous change in ΔA .

VII. SUMMARY

In summary, we have systematically studied the shapes of low energy and, in this way, determined the phase diagram for two variants of the curvature model. In this model, the shape of a fluid vesicle is determined by the minimum of the bending energy under additional constraints for the area, the enclosed volume, and the integrated mean curvature of the spontaneous curvature. In order to obtain a general overview over the shapes, it was appropriate to relax the constraints and, thus, to consider the problem of extremal energy for given "fields," i.e., for a given external tension, pressure difference, and spontaneous curvature. The solutions to the shape equations for axisymmetric vesicles can be classified into branches. We discussed in detail the prolate-dumbbell, the pear-shaped, the oblate-discocyte,

and the stomatocyte branches.

Quite generally, branches emerge and vanish either (i) at bifurcations or (ii) at limit points. *Bifurcations* result from successive symmetry breaking. The shape of highest symmetry is the sphere. Its rotational invariance can be broken with $Y^{l,m}$ perturbations. The shapes which result from an even l perturbation have up-down symmetry like the prolate and oblate ellipsoids for $l=2$. Breaking this symmetry leads to asymmetric vesicles like the pear shapes and the stomatocytes. *Limit points* are points beyond which the branches cannot be extended. We may distinguish three types of limit shapes: (i) Shapes where the volume becomes infinite like the capped cylinders which are limit points for the prolate-dumbbell shapes. (ii) Shapes which consist of two or several parts connected by an infinitesimal neck. For the pear-shaped vesicles, these limit shapes correspond to the budding phenomenon. The occurrence of these limit shapes is generally restricted to those which fulfill the relation (3.14) between the curvatures of the adjacent shapes and the spontaneous curvature. (iii) Shapes for which two segments of the membrane start to self-intersect and the model becomes unphysical.

We then imposed constraints to the surface area and the enclosed volume, i.e., we searched for the shape of lowest bending energy for a given area and volume. Two variants can be considered which are related via a Legendre transformation. These are the spontaneous-curvature model and the bilayer-coupling model. Shapes which correspond to a local minimum in one model may, however, correspond to a saddle point and are therefore unstable in the other model. This has been discussed in terms of energy diagrams, as in Figs. 4 and 8. As a general feature, we find that the transitions in the bilayer-coupling model are *continuous* while those in the spontaneous-curvature model are *discontinuous* (with one exception) because in the latter model the branches typically develop “wings” with unstable and metastable parts. This distinction should have important consequences, since, e.g., in the spontaneous-curvature model, hysteresis effects at the discontinuous transitions are expected. We compared the energy of the different branches and, thus, determined the phase diagrams for both models. While half of the phase diagram of the bilayer-coupling model shown in Fig. 3 was already known, the phase diagram for the spontaneous-curvature model displayed in Fig. 10 is new and constitutes one of our main results.

For a comparison between theory and experiment, we introduced trajectories into these phase diagrams (see Fig. 15). A temperature trajectory determines the sequence of shapes and transformations which result from a change in temperature. For the bilayer-coupling model, we found that already a minute asymmetry in the monolayer expansivities has drastic consequences. If the expansivity of the outer monolayer is larger than the expansivity of the inner one, typically budding will occur, while in the reverse situation the inclusion of a small cavity is predicted. Although for the spontaneous-curvature model a similar detailed analysis is difficult since the temperature dependence of the spontaneous curvature is not obvi-

ous, we could discuss the similarities and differences in both models for typical trajectories, such as a reentrant trajectory (Figs. 11 and 12), a budding trajectory (Figs. 13 and 14), and the oblate-stomatocyte transition (Figs. 8 and 9). As a main result, we find that both models typically lead to different predictions. This also holds for trajectories which are induced by changing the osmotic conditions.

In conclusion, we provided a detailed study of vesicle shapes and their transformations which should enable an experimental test between both variants of the model. Since different *physical* assumptions lie behind these variants, any experiment which can distinguish between the predictions of the two models will improve our understanding of these bilayer systems. A recent experiment on the shape transformations of giant dimyristoyl phosphatidylcholine (DMPC) vesicles gave good agreement with the theoretical predictions obtained from the bilayer-coupling model [31]. More experiments on different systems are certainly required to obtain a general picture. We hope that our theoretical study will provide some guidance for these experiments.

During the preparation of this manuscript we obtained copies of several papers prior to publication that were concerned with some aspects of our work: Budding in the spontaneous-curvature model has also been considered by Wiese and Helfrich [38] and for large spontaneous curvature by Miao *et al.*, [39]; pear-shaped states in the bilayer-coupling model have been independently found by Svetina, Kralj-Iglic, and Zeks [40]; and the oblate-stomatocyte transition in the spontaneous-curvature model has also been studied by Peterson [41].

ACKNOWLEDGMENTS

We thank J. Käs and E. Sackmann for enjoyable collaboration. Stimulating discussions with E. Evans, B. Fourcade, W. Helfrich, M. Peterson, and M. Wortis are gratefully acknowledged. We thank M. Peterson, W. Wiese and W. Helfrich, and S. Svetina, V. Kralj-Iglic, and B. Zeks for sending us copies of papers prior to publication. This work was supported by the Deutsche Forschungsgemeinschaft through the Sonderforschungsbereich No. 266.

APPENDIX A: REFERENCE SURFACE

In this appendix we discuss (i) a possible definition of the reference surface for the bilayer-coupling model in terms of the two monolayers [42], (ii) the irrelevance of the spontaneous curvature in the bilayer-coupling model, and (iii) the thermal expansivity of the reference surface if the two monolayers expand asymmetrically.

We start from a continuum model for the two monolayers at constant separation D . Their bending energy is given by

$$F_b^j = (\kappa^j/2) \oint dA^j (2H^j - C_0^j)^2 + \kappa_G^j \oint dA^j K^j, \quad (\text{A1})$$

where $j = \text{in}$ or ex refers to the two monolayers. Here A^j is the area, $H^j \equiv (C_1^j + C_2^j)/2$ the mean, and $K^j \equiv C_1^j C_2^j$ the Gaussian curvature, κ^j and κ_G^j are the bending rigidities and C_0^j is the spontaneous curvature of the two

monolayers, respectively.

We now introduce a reference surface with area A , mean curvature H , and Gaussian curvature K which is in a fixed but yet undetermined distance βD from the inner monolayer. Using standard formulas of differential geometry, one has

$$dA^{\text{in}} \approx dA(1 - 2D\beta H), \quad (\text{A2})$$

$$dA^{\text{ex}} \approx dA[1 + 2D(1 - \beta)H], \quad (\text{A3})$$

$$H^{\text{in}} \approx H + D\beta(2H^2 - K), \quad (\text{A4})$$

$$H^{\text{ex}} \approx H - (1 - \beta)D(2H^2 - K), \quad (\text{A5})$$

$$K^{\text{in}} \approx K + 2D\beta HK, \quad (\text{A6})$$

and

$$K^{\text{ex}} \approx K - 2D(1 - \beta)HK, \quad (\text{A7})$$

up to order D^2/A . Inserting these expressions into (A1), one observes that the total bending energy $F_b = F_\kappa^{\text{in}} + F_\kappa^{\text{ex}}$ can be written in the form

$$\begin{aligned} F_\kappa^{\text{in}} + F_\kappa^{\text{ex}} = & (\kappa/2) \left[\oint dA(2H - C_0)^2 \right. \\ & \left. + \text{const } A + O\left[\frac{D^2}{A}\right] \right] \\ & + \kappa_G \left[\oint dA K + O\left[\frac{D^2}{A}\right] \right], \quad (\text{A8}) \end{aligned}$$

provided one chooses

$$\beta = \kappa^{\text{ex}} / (\kappa^{\text{in}} + \kappa^{\text{ex}}), \quad (\text{A9})$$

which determines the position of the reference surface. Moreover, one has to define

$$\kappa \equiv \kappa^{\text{in}} + \kappa^{\text{ex}}, \quad (\text{A10})$$

$$\kappa_G \equiv \kappa_G^{\text{in}} + \kappa_G^{\text{ex}} + 4D[\beta\kappa^{\text{in}}C_0^{\text{in}}/2(1 - \beta)\kappa^{\text{ex}}C_0^{\text{ex}}/2], \quad (\text{A11})$$

$$\begin{aligned} C_0 \equiv & (\kappa^{\text{in}}C_0^{\text{in}} + \kappa^{\text{ex}}C_0^{\text{ex}})/\kappa \\ & + (D/\kappa)[\beta\kappa^{\text{in}}(C_0^{\text{in}})^2/2 - (1 - \beta)\kappa^{\text{ex}}(C_0^{\text{ex}})^2/2]. \quad (\text{A12}) \end{aligned}$$

Ignoring the terms of order D^2/A , one arrives at (2.1) for the bending energy in the spontaneous-curvature model.

In the bilayer-coupling model, the area difference

$$\Delta A = A^{\text{ex}} - A^{\text{in}} \approx 2DM \equiv 2D \oint H dA \quad (\text{A13})$$

is prescribed. In this case, however, the spontaneous curvature C_0 occurring in (A8) is irrelevant, as can be seen from the identities

$$\begin{aligned} \min_{A, V, M} (F_\kappa^{\text{in}} + F_\kappa^{\text{ex}}) &= \min_{A, V, M} \left[\frac{\kappa}{2} \oint dA (2H)^2 \right. \\ & \quad \left. - 2\kappa C_0 M + \frac{\kappa}{2} C_0^2 A \right] \\ &= \min_{A, V, M} \left[\frac{\kappa}{2} \oint dA (2H)^2 \right] \\ &= \min_{A, V, M} G_b, \quad (\text{A14}) \end{aligned}$$

with G_b as in (2.3). Therefore, the spontaneous curvature can be ignored in the bilayer-coupling model from the very beginning. Stated differently, the phase diagram in the bilayer-coupling model does not depend on a spontaneous curvature.

Let us finally discuss the consequences of an asymmetric expansion of the monolayers in this approach. We need in Sec. VI the thermal expansivity of the reference surface in the bilayer-coupling model. This quantity is given by

$$\begin{aligned} \left[\frac{dA}{dT} \right] / A & \approx \left[\frac{d[(1 - \beta)A^{\text{in}} + \beta A^{\text{ex}}]}{dT} \right] / [(1 - \beta)A^{\text{in}} + \beta A^{\text{ex}}] \\ & \approx \alpha(1 + \beta\gamma), \quad (\text{A15}) \end{aligned}$$

up to

$$O(\gamma^2, \gamma(\Delta A/A), (\Delta A/A)^2).$$

Here, we used the expansivities (6.1) for the two monolayers. Therefore, $\bar{\gamma}$ of (6.2) is given by

$$\bar{\gamma} = \beta\gamma. \quad (\text{A16})$$

For this derivation, we assumed that κ^{in} and κ^{ex} are temperature independent.

APPENDIX B: ALGORITHM

In this appendix we describe the algorithm we use in order to solve the shape equations (3.5).

In principle, a complete set of solutions can be obtained as follows: First, choose $\bar{P} > 0$ which defines a length scale $\bar{P}^{-1/3}$ and fix $\bar{\Sigma}$ and C_0 . Then, integrate the differential equations (3.5) with the initial values $\psi(0) = 0$, $U(0) = 0$, $X(0) = 0$, and $\gamma(0) = 0$. Now, define $S_1^{(n)}$ by $\psi(S_1^{(n)}) = \pi$ with $n \geq 1$ and $S_1^{(n+1)} > S_1^{(n)}$. A plot of $X(S_1^{(n)})$ versus $U(0)$ is shown in Fig. 16. The values $\bar{U}(0)$ and $\bar{S}_1^{(n)}$ for which $S(\bar{S}_1^{(n)}) = 0$ yield solutions of the shape equations (3.5) with the boundary conditions (3.6)–(3.8). Note, that $\gamma(S_1) = 0$ is automatically fulfilled for $U(0) = \bar{U}(0)$ because H is conserved.

Since $X = 0$ is a *singular* point of the equations (3.5), $X(S_1^{(n)}) = 0$ cannot really be reached numerically. Therefore, it is in practice better to determine an approximative value $U(0)^*$ for $\bar{U}(0)$ by extrapolation from the values obtained by a diagram like Fig. 16. Likewise, one obtains from this approximate solution an estimate $S_1^{(n)*}$

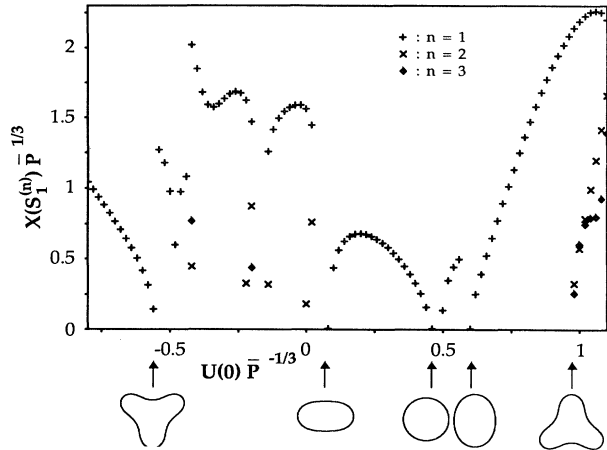


FIG. 16. Systematic search for solutions to the shape equation for $\bar{\Sigma} = -1.1\bar{P}^{2/3}$ and $C_0 = 0$. Solutions are obtained for those $U(0)$ for which $X(S_1^{(n)}) = 0$. The corresponding shapes are displayed. The solutions can typically be attained from one side of the $U(0)$ axis. If a trial contour has reached one of the following stopping criteria: $X(S_1^{(n)})P^{-1/3} < 10^{-2}$, $\Psi(S) < -2\pi$, $\Psi(S) > 3\pi$, or maximal 1.6×10^{-5} integration steps of maximal step size 10^{-3} , it was discarded without marking.

to $\bar{S}_1^{(n)}$ and an estimate U_1^* to the curvature at the south pole $\bar{U}_1 \equiv U(\bar{S}_1^{(n)})$. These estimates are then used as initial values in a shooting method, as follows:

Choose this value $U(0)^*$, integrate a fixed length $\bar{S} < S_1^{(n)*}$ from the north pole at $S=0$ and obtain $\psi(\bar{S})$, $U(\bar{S})$, $X(\bar{S})$, and $\gamma(\bar{S})$. Then start a second integration at the south pole with $U = U_1^*$, integrate (backwards) from $S_1^{(n)}$ a length $\hat{S} = S_1^{(n)*} - \bar{S}$, and obtain $\psi'(\bar{S})$, $U'(\bar{S})$, $X'(\bar{S})$, and $\gamma'(\bar{S})$. Finally, one has to adjust the parameters $U(0)^*$, U_1^* and $S_1^{(n)*}$ in order to fulfill $\psi(\bar{S}) = \psi'(\bar{S})$, $U(\bar{S}) = U'(\bar{S})$, and $X(\bar{S}) = X'(\bar{S})$. Since H is conserved, $\gamma(\bar{S}) = \gamma'(\bar{S})$ is then automatically satisfied.

This procedure must be repeated for any value of $\bar{\Sigma}$ and C_0 . The absolute value of the chosen $\bar{P} > 0$ is irrelevant, since it sets only the basic length scale. Therefore, it is sufficient to repeat the above-mentioned procedure with a fixed but arbitrary $\bar{P} < 0$ and finally with $\bar{P} = 0$. In the latter case, the length scale is set by $|\bar{\Sigma}|^{-1/2}$ or $|C_0|^{-1}$.

If one solution has been found for certain values of \bar{P} , $\bar{\Sigma}$, and C_0 , it is relatively simple to keep track of this solution under a small change in $\bar{\Sigma}$ and C_0 . In this way, we obtained the branches of stationary shapes shown in Sec. III C and Fig. 2.

For the determination of the phase diagram it is more convenient to work directly in a space where A , V , and C_0 or M are fixed. To this end, we augment the shape equations (3.5) with two more equations for the area A and volume V which read

$$\dot{A} = 2\pi X \quad (\text{B1a})$$

and

$$\dot{V} = \pi X^2 \sin \psi, \quad (\text{B1b})$$

with the boundary values

$$A(0) = 0, \quad (\text{B2a})$$

$$A(S_1) = A_1, \quad (\text{B2b})$$

$$V(0) = 0, \quad (\text{B2c})$$

and

$$V(S_1) = V_1. \quad (\text{B2d})$$

These equations have to be solved together with the shape equations (3.5), by adjusting the free parameters $U(0)$, S_1 , \bar{P} , and $\bar{\Sigma}$. For any shape found by the method described above, these parameters can be determined for any prescribed area by simple rescaling. It is then relatively easy to vary, e.g., V while keeping A_1 and C_0 fixed and, thus, to investigate the behavior of a certain branch as a function of V . Likewise, C_0 can be varied for fixed V_1 . This holds in the spontaneous-curvature model.

In the bilayer-coupling model, the integrated mean curvature M is also controlled which leads to one more differential equation,

$$\dot{M} = \pi(XU + \sin \psi), \quad (\text{B3})$$

with the boundary conditions

$$M(0) = 0 \quad (\text{B4a})$$

and

$$M(S_1) = M_1, \quad (\text{B4b})$$

and free C_0 . In this way, we have determined the phase diagrams given in Secs. IV and V.

APPENDIX C: PROOF OF (4.8)

In this appendix we sketch the proof of (4.8). For a deformed sphere as parametrized in (3.10), the area $A(a_{l,m})$ and volume $V(a_{l,m})$ are given explicitly in (51) and (52) of Ref. [33] as

$$A(a_{l,m}) - A(0) \approx 2\sqrt{4\pi}a_{0,0}R_0 + \sum_{l,m} |a_{l,m}|^2 [1 + l(l+1)/2] \quad (\text{C1})$$

and

$$V(a_{l,m}) - V(0) \approx \sqrt{4\pi}a_{0,0}R_0^2 + R_0 \sum_{l,m} |a_{l,m}|^2. \quad (\text{C2})$$

The \approx throughout this appendix means up to order $a_{l,m}^3$. Using the formulas for the second variation of the area and mean curvature given in Ref. [33], it is straightforward to derive that the integrated mean curvature M is given by

$$M(a_{l,m}) - M(0) \approx \sqrt{4\pi}a_{0,0} + (2R_0)^{-1} \sum_{l,m} |a_{l,m}|^2 l(l+1). \quad (\text{C3})$$

Since we fix the area, $A(a_{l,m}) \approx A(0)$, we have from (C1)

$$\sqrt{4\pi}a_{0,0} \approx -(2R_0)^{-1} \sum_{l,m} |a_{l,m}|^2 [1 + l(l+1)/2]. \quad (\text{C4})$$

Inserting this relation in Eqs. (C2) and (C3), we have

$$M(a_{l,m}) - M(0) \approx -R_0^{-2} [V(a_{l,m}) - V(0)]. \quad (\text{C5})$$

With the definitions (4.1)–(4.3) for the reduced variables Δa and v , we find finally

$$\left. \frac{d\Delta a}{dv} \right|_{v=1} = (R_0^2/3) \left. \frac{dM}{dV} \right|_{V=4\pi R_0^3/3} = -\frac{1}{3}. \quad (\text{C6})$$

This result shows that in the spherical limit $v \rightarrow 1$, the variations of M and V are not independent.

APPENDIX D: DERIVATION OF THE PHASE DIAGRAM FOR THE SPONTANEOUS-CURVATURE MODEL

In this appendix we sketch the derivation of the phase diagram in the spontaneous-curvature model, as shown in Fig. 10. First, we deal with the oblate-discocyte and stomatocyte branches. In Fig. 17 we show the functional dependence of the bending energy $F_b(v)$ for $c_0 = -2$. The stomatocytes bifurcate at $v = v_C^{\text{sto}}$ from the oblate branch and reach their maximal volume at $v = v_M^{\text{sto}}$. This part of the stomatocyte branch is locally unstable, as has been explained in Sec. V A for $c_0 = 0$. The locally stable stomatocytes end at the limit shape L^{sto} . This holds for $c_0 < 0$. For $c_0 > 0$, the locally stable part of the stomatocyte branch terminates at $v = v_{SI}^{\text{sto}}$, where the shapes self-intersect. In Fig. 18(a), we show the lines C^{sto} , M^{sto} , L^{sto} , and SI^{sto} in the (c_0, v) plane. Locally stable stomatocytes exist in a region bounded by M^{sto} , L^{sto} , and SI^{sto} . This region is divided into two parts by the line D^{sto} which denotes the discontinuous transition between the oblate-discocyte shapes and the stomatocytes. Below D^{sto} , in the shaded region, the stomatocytes have lowest bending energy. Above D^{sto} , the stomatocytes are metastable and the oblate-discocyte shapes have lower bending energy. At the line SI^{ob} , the latter shapes self-intersect. We also display an approximation to the oblate-stomatocyte transition denoted by $D^{*\text{sto}}$ and discussed in Appendix E.

The oblate-discocyte branch also develops a ‘‘wing,’’ as displayed in Fig. 17. Although this wing has no conse-

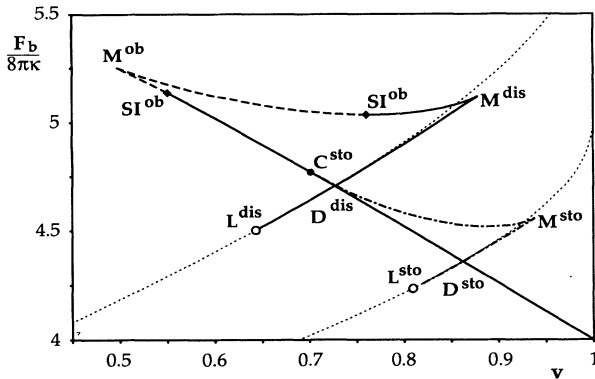


FIG. 17. Bending energy of the oblate, the stomatocyte, and the discocyte-2 branches for $c_0 = -2$. At C^{sto} , the unstable part of the stomatocytes (dashed-dotted line) bifurcates from the oblate branch. Between L^{sto} and M^{sto} , the stomatocytes are locally stable. The oblate branch reaches its minimal volume at M^{ob} and is locally unstable between M^{ob} and M^{dis} . The locally stable part between M^{dis} and L^{dis} is called discocyte-2. Between the points denoted with SI^{ob} , the shapes are self-intersected. D^{sto} and D^{dis} denote discontinuous transitions. The dotted lines give approximations to the discocytes-2 and the stomatocytes, as discussed in Appendix E.

quences for the phase diagram, we discuss it for completeness. The oblate-discocyte branch reaches at $v = v_M^{\text{ob}}$ its minimal volume. The upper part of the wing, with $v_M^{\text{ob}} < v < v_M^{\text{dis}}$, corresponds to locally unstable shapes. For $v < v_M^{\text{dis}}$, we call the locally stable shapes of this branch discocytes-2. With decreasing volume, this branch terminates at a limit shape L^{dis} which consists of two inverted spheres of radii $R_1 < 0$ embedded in a larger sphere with radius $R_2 > 0$ and connected by ideal necks. The loci of these shapes are determined by the relations

$$2R_1^2 + R_2^2 = R_0^2, \quad 2R_1^3 + R_2 = vR_0^3$$

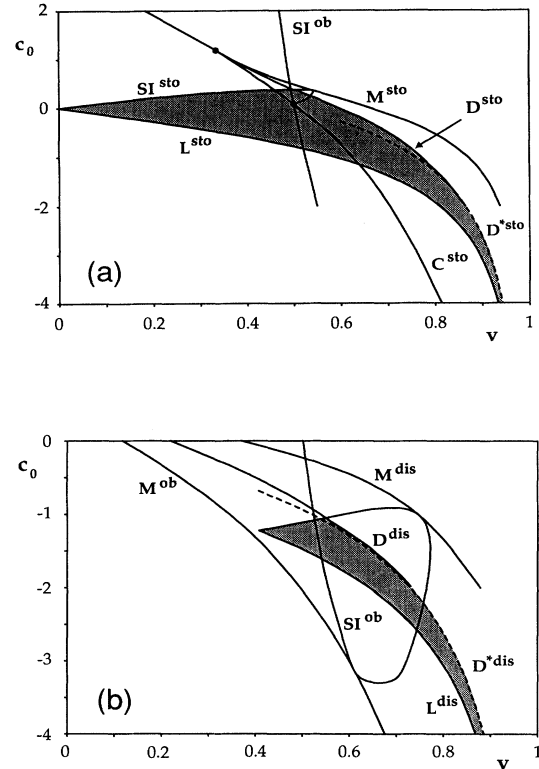


FIG. 18. Lines in the (c_0, v) plane required for the derivation of the phase diagram of the c_0 model. (a) Lines related to the stomatocytes which have lowest energy in the shaded region. C^{sto} , M^{sto} , and L^{sto} denote lines where the stomatocytes bifurcate from the oblate branch, reach their maximal volume, and end up in the limit shape, respectively. D^{sto} denotes the transition between the oblates and the stomatocytes. $D^{*\text{sto}}$ is an approximation to these transitions, as discussed in Appendix E. On the left-hand side of the line SI^{ob} , the oblates are self-intersected. The point where the three lines C^{sto} , D^{sto} , and M^{sto} merge corresponds to a tricritical point. It is, however, in the region of self-intersected shapes. (b) Lines related to the discocytes which are locally stable in the shaded regions. M^{ob} and M^{dis} denote the lines of minimal and maximal volume of the unstable part. L^{dis} denotes the limit point for the discocytes-2 which exist between M^{dis} and L^{dis} . SI^{ob} denotes the points of self-intersection. D^{dis} gives the transition between the discocytes-2 and the oblates. $D^{*\text{dis}}$ denotes the approximation to this transition, as discussed in Appendix E.

and

$$R_1^{-1} + R_2^{-1} = C_0. \quad (D1)$$

This holds for $c_0 < -\sqrt{3}/2$. For $c_0 = -\sqrt{3}/2$, the radii of the inverted spheres are given by $R_1 = R_2/2$ and, thus, the inverted spheres touch each other. For $c_0 > -\sqrt{3}/2$, the discocyte-2 branch therefore already terminates at the point SI^{dis} , where the shape self-intersects. As shown in Appendix E, this discocyte-2 branch lies above the locally stable stomatocyte branch for all $v > v_L^{\text{sto}}$ and all values of c_0 . Therefore, no transition between these two locally stable branches occurs and the discocytes-2 do not show up in the phase diagram. In Fig. 18(b) we display the lines M^{ob} , M^{dis} , L^{dis} , and SI^{dis} in the (c_0, v) plane. Moreover, we include the line D^{dis} where the discocyte-2 branch crosses the oblate-discocyte branch. The line $D^{*\text{dis}}$ is an approximation to this line discussed in Appendix E.

We now turn to the prolate-dumbbell and to the pear-shaped states (compare Fig. 10). For $c_0 \lesssim 1.92$, the energy of the prolate branch decreases monotonically with v , while for $c_0 \gtrsim 1.92$ two extrema develop. In Fig. 19 we display a schematic energy diagram valid for $c_0^{(1)} < c_0 < c_0^{(2)}$, with $c_0^{(1)} \simeq 2.063$ and $c_0^{(2)} \simeq 2.066$. Apart from the prolate-dumbbell branch which starts at the sphere, an additional branch of symmetric solutions has emerged, which we call prolate-*b*. The lower part of this branch originates from the limiting shape B_2 at $v = \sqrt{2}/2$, where two spheres of equal radii are connected by an ideal neck. This prolate-*b* branch has a minimal volume $v = v_M^{\text{pro}} < \sqrt{2}/2$. The energy of the upper part increases while the shape approaches presumably a new type of limiting shape where two spheres are joined by a neck that contains energy. We find numerically that the pressure P of this solution diverges as $P \sim (\sqrt{2}/2 - v)^{-1}$. Since

$$P = - \left. \frac{\partial F_b}{\partial V} \right|_{A, C_0},$$

this would indicate a logarithmic divergence of the bending energy F_b . The numerical calculation of shapes belonging to this branch, however, is very cumbersome. Therefore, it is also difficult to determine for which value of $c_0 = c_0^*$ these shapes occur for the first time. We can only give the (presumably bad) upper bound $c_0^* < 1.7$. From an investigation of these shapes in the $(\bar{\Sigma}, \bar{P})$ ensemble, we expect $c_0^* \geq 0$.

For $c_0 = c_0^{(2)}$, with $c_0^{(2)} \simeq 2.066$, the prolate-*b* branch touches the prolate branch which starts at the sphere. For $c_0 > c_0^{(2)}$, both branches rearrange, as shown in Fig. 11 for $c_0 = 2.4$. We call prolate-1 the branch that originates in the sphere, has a minimal volume $v_M^{\text{pro}} < \sqrt{2}/2$, and approaches the limit shape with nonideal neck for $v \rightarrow \sqrt{2}/2$ from below. We call the other branch that originates in the limit shape B_2 , prolate-2. For $v = v_B^{\text{pro}}$ the lower part of the prolate-1 branch crosses the prolate-2 branch. This leads to a discontinuous transition D^{pro} between two different symmetric shapes.

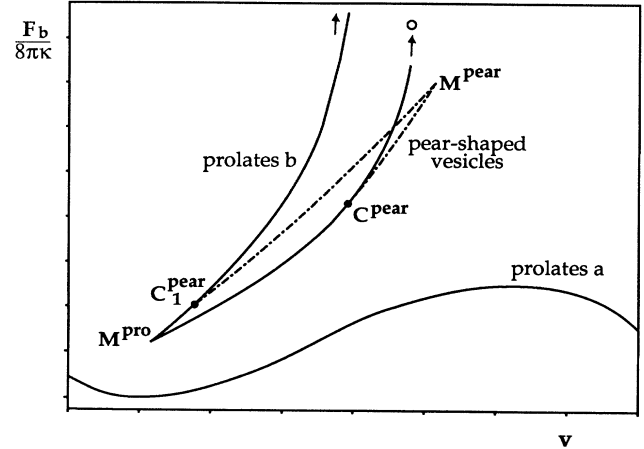


FIG. 19. Schematic energy diagram for $c_0^{(1)} < c_0 < c_0^{(2)}$, with $c_0^{(1)} \simeq 2.063$ and $c_0^{(2)} \simeq 2.066$. The prolate-*a* branch corresponds to the prolates which start at the sphere for $v=1$ and approaches a long thin capped cylinder for $v \rightarrow 0$. The lower part of the prolate-*b* branch starts at a limit shape where two spheres of equal radii are connected by an ideal neck. The energy of the upper part presumably diverges for $v \rightarrow \sqrt{2}/2$. Both branches show an instability with respect to the up-down symmetry. For $c_0 < c_0^{(1)}$, the asymmetric branch has not yet emerged.

In Fig. 20 we show the lines M^{pro} and D^{pro} in the (c_0, v) plane. This figure also contains additional lines which will be defined below and refer to the asymmetric pear-shaped vesicles.

These pear-shaped states arise from an instability with

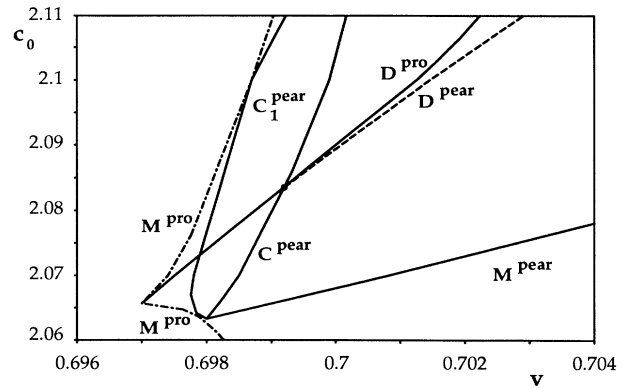


FIG. 20. Lines in the (c_0, v) plane related to the transition between different prolates and the occurrence of the pear-shaped states. M^{pro} denotes the minimal volume for the prolate-*b* and the prolate-1 branch. The cusp in this line corresponds to the rearrangement of the prolate branches. The solid line D^{pro} gives the transition between the two prolate branches. C^{pear} and C_1^{pear} denote the lines where the pear-shaped vesicles bifurcate from the prolates. M^{pear} denotes the maximal volume for the pear-shaped vesicles. The dashed line D^{pear} gives the discontinuous transition between the pear-shaped and the prolate-1 branches.

respect to the up-down symmetry of the prolate- b branch for $c_0 = c_0^{(1)}$ with $c_0^{(1)} \simeq 2.063$. In fact, both parts of this branch develop an instability. The upper part develops this instability for $v = v_{\mathcal{L}_1}^{\text{pear}}$ while the lower part becomes unstable for $v = v_{\mathcal{L}}^{\text{pear}}$ (compare the schematic energy diagram, Fig. 19.) The two asymmetric pear-shaped branches which arise from these instabilities meet for $v = v_M^{\text{pear}}$. Thus locally stable pear-shaped vesicles exist for $v_{\mathcal{L}}^{\text{pear}} < v < v_M^{\text{pear}}$ (compare Fig. 20).

The line D^{pro} denotes the discontinuous transition between the two prolate branches in the narrow region with $c_0^{(2)} < c_0 < c_0^{(3)}$. The value $c_0^{(3)} \simeq 2.08$ is defined by the intersection of the lines C^{pear} and D^{pro} . For $c_0 > c_0^{(3)}$, the line D^{pear} denotes a discontinuous transition between the prolate-1 branch and the pear-shaped branch (compare Fig. 11). Therefore, metastable pear-shaped states exist in a region bounded by the lines M^{pear} , C^{pear} , and D^{pear} (compare Fig. 20). With increasing c_0 , these lines shift to larger v values. In fact, M^{pear} and D^{pear} approach $v = 1$ for $c_0 \rightarrow \infty$ while C^{pear} terminates at the point B_2 with $(c_0, v) = (2\sqrt{2}, \sqrt{2}/2)$. For $c_0 = 2\sqrt{2}$ the energy of the limiting shape B_2 vanishes. For even larger values of c_0 , the prolate-2 and the pear-shaped branches are no longer connected because the pear-shaped states reach their limiting shape L^{pear} at $v = v_L^{\text{pear}}$ with $v_L^{\text{pear}} > \sqrt{2}/2$ given by (5.4). Likewise, the prolate-2 branch starts at the limit shape L^{dumb} , with $v_L^{\text{dumb}} < \sqrt{2}/2$ where two prolate ellipsoids are connected by an ideal neck. Compare Figs. 13 and 14 for $c_0 = 3$.

APPENDIX E: APPROXIMATION TO DISCONTINUOUS TRANSITIONS

For $|c_0| \gg 1$, the computation of the pear-shaped states and the stomatocytes with a narrow neck becomes increasingly time consuming. The bending energy of these shapes is necessary in order to determine the phase boundaries D^{pear} and D^{sto} . It is therefore helpful to discuss a simple approximation to these boundaries which, however, becomes asymptotically exact for $|c_0| \rightarrow \infty$. To this end one has to approximate the bending energies of the two branches whose intersection leads to the discontinuous transition. We first discuss this approximation for the D^{pear} line. We approximate the energy of the pear-shaped vesicles $F_b(v)$ by the energy of two spheres F_b^* , with

$$F_b^*(v) \equiv 2\pi\kappa[(2 - C_0 R_1)^2 + (2 - C_0 R_2)^2], \quad (\text{E1})$$

with $R_1^2 + R_2^2 = R_0^2$ and $R_1^3 + R_2^3 = vR_0^3$. A short calcula-

tion shows that $F_b(v) \approx F_b^*(v)$ up to order $(v - v_L^{\text{pear}})^2$. Therefore, F_b^* is a good approximation to the energy for the pear-shaped states for the whole range $v_L^{\text{pear}} < v < v_M^{\text{pear}}$, as displayed in Fig. 13 for $c_0 = 3$. The energy of the prolate-dumbbell shapes is approximated by F_b^{lin} , with

$$F_b^{\text{lin}}(v) \equiv F_b(1) + \left. \left[\frac{\partial F_b}{\partial v} \right] \right|_{v=1} (v - 1). \quad (\text{E2})$$

The derivative $(\partial F_b / \partial v)|_{v=1}$ can be expressed by the critical pressure $\bar{P}_{c,2}$ (3.11), which leads to

$$\begin{aligned} \left. \left[\frac{\partial F_b}{\partial v} \right] \right|_{v=1} &= -(4\pi/3)R_0^3 P_{c,2} \\ &= -(4\pi/3)2\kappa(6 - c_0). \end{aligned} \quad (\text{E3})$$

Inserting (E3) in (E2) leads to

$$F_b^{\text{lin}}(v) = 8\pi\kappa[(1 - c_0/2)^2 - (6 - c_0)(v - 1)/3]. \quad (\text{E4})$$

Once again, we have $F_b(v) \approx F_b^{\text{lin}}(v)$ up to order $(1 - v)^2$. The approximation $v_D^{*\text{pear}}$ for the prolate pear-shaped transition is now defined by

$$F_b^*(v_D^{*\text{pear}}) = F_b^{\text{lin}}(v_D^{*\text{pear}}).$$

This line has been displayed in Fig. 10. The same arguments can be used for an approximation to the discontinuous transition D^{sto} . In fact, (E1) holds also as an approximation to the energy of the stomatocytes with $R_1 < 0$ and $C_0 < 0$, as already displayed in Fig. 17, and Eq. (E4) is also valid for the energy of the oblates up to order $(v - 1)^2$. Comparing both approximate energies leads to the approximation $v_D^{*\text{sto}}$, as displayed in Fig. 10.

The approximation $D^{*\text{dis}}$ for the intersection between the discocyte-2 and the oblate-discocyte branches displayed in Fig. 18(b) has been obtained along similar lines. We approximate the energy of the discocytes-2 by the energy of three spheres F_b^{**} , with

$$F_b^{**}(v) \equiv 2\pi\kappa[2(2 - C_0 R_1)^2 + (2 - C_0 R_2)^2], \quad (\text{E5})$$

with $R_1 < 0$, $2R_1^2 + R_2^2 = R_0^2$, and $2R_1^3 + R_2^3 = vR_0^3$. This function has also been displayed in Fig. 17. The approximation $v_D^{*\text{dis}}$ for the oblate-discocyte-2 transition is now defined by $F_b^{**}(v_D^{*\text{dis}}) = F_b^{\text{lin}}(v_D^{*\text{dis}})$. With (E1) and (E5) one can, moreover, estimate the location of a transition between discocytes-2 and stomatocytes. It turns out that $v_D^{*\text{dis}}(c_0) < v_L^{\text{sto}}(c_0)$ for all $c_0 < 0$. Therefore, no transitions between stomatocytes and discocytes-2 occur.

*Present address: Department of Physics, Simon Fraser University, Burnaby, British Columbia, Canada V5A 1S6.

†New address: Institut für Festkörperphysik, Forschungszentrum Jülich, 5170 Jülich, Federal Republic of Germany.

[1] *Physics of Amphiphilic Layers*, edited by J. Meunier, D. Langevin, and N. Boccardo, Springer Proceedings in Phys-

ics Vol. 21 (Springer, Berlin, 1987).

[2] Proceedings of the Conference on Fluctuations in Lamellae and Membranes, Miami, 1989 [Langmuir (to be published)].

[3] Proceedings of the Thirteenth International Liquid Crystals Conference, Vancouver, 1990 [Mol. Cryst. Liq. Cryst. (to be published)].

- [4] E. Sackmann, H. P. Duwe, and H. Engelhardt, *Faraday Discuss. Chem. Soc.* **81**, 281 (1986).
- [5] E. Sackmann, H. P. Duwe, K. Zeman, and A. Zilker, in *Structure and Dynamics of Nucleic Acids, Proteins and Membranes*, edited by E. Clementi and S. Chin (Plenum, New York, 1986), p. 251.
- [6] H. P. Duwe, J. Käs, and E. Sackmann, *J. Phys. (Paris)* **51**, 945 (1990).
- [7] E. Evans and W. Rawicz, *Phys. Rev. Lett.* **64**, 2094 (1990).
- [8] M. B. Schneider, J. T. Jenkins, and W. W. Webb, *J. Phys. (Paris)* **45**, 1457 (1984).
- [9] H. Engelhardt, H. P. Duwe, and E. Sackmann, *J. Phys. Lett. (Paris)* **46**, L395 (1985).
- [10] I. Bivas, P. Hanusse, P. Bothorel, J. Lalanne, and O. Aguerre-Chariol, *J. Phys. (Paris)* **48**, 855 (1987).
- [11] J. F. Faucon, M. D. Mitov, P. Méléard, I. Bivas, and P. Bothorel, *J. Phys. (Paris)* **50**, 2389 (1989).
- [12] E. Evans and D. Needham, *J. Phys. Chem.* **91**, 4219 (1987).
- [13] E. Evans, *Colloids and Surfaces* **43**, 327 (1990).
- [14] L. Bo and R. Waugh, *Biophys. J.* **55**, 509 (1989).
- [15] P. B. Canham, *J. Theoret. Biol.* **26**, 61 (1970).
- [16] W. Helfrich, *Z. Naturforsch, Teil C* **28**, 693 (1973).
- [17] E. Evans, *Biophys. J.* **14**, 923 (1974).
- [18] H. J. Deuling and W. Helfrich, *J. Phys. (Paris)* **37**, 1335 (1976).
- [19] J. T. Jenkins, *J. Math. Biology* **4**, 149 (1977).
- [20] J. C. Luke, *SIAM J. Appl. Math.* **42**, 333 (1982).
- [21] J. C. Luke and J. I. Kaplan, *Biophys. J.* **25**, 107 (1979).
- [22] M. A. Peterson, *J. Appl. Phys.* **57**, 1739 (1985).
- [23] J. Verhas, *Liquid Crystals* **3**, 1183 (1988).
- [24] S. Svetina and B. Zeks, *Biomed. Biochim. Acta* **42**, 86 (1983).
- [25] S. Svetina and B. Zeks, *Eur. Biophys. J.* **17**, 101 (1989).
- [26] M. A. Peterson, *Mol. Cryst. Liq. Cryst.* **127**, 257 (1985).
- [27] S. T. Milner and S. A. Safran, *Phys. Rev. A* **36**, 4371 (1987).
- [28] U. Seifert and R. Lipowsky, *Phys. Rev. A* **42**, 4768 (1990).
- [29] R. Lipowsky and U. Seifert, in Refs. [2] and [3].
- [30] M. P. Sheetz and S. J. Singer, *Proc. Natl. Acad. Sci. (U.S.A.)* **71**, 4457 (1974).
- [31] K. Berndl, J. Käs, R. Lipowsky, E. Sackmann, and U. Seifert, *Euro. Phys. Lett.* **13**, 659 (1990).
- [32] Ou-Yang Zhong-can and W. Helfrich, *Phys. Rev. Lett.* **59**, 2486 (1987).
- [33] Ou-Yang Zhong-can and W. Helfrich, *Phys. Rev. A* **39**, 5280 (1989).
- [34] M. A. Peterson, *Phys. Rev. A* **39**, 2643 (1989).
- [35] In our previous letter, Ref. [31], we have shown a line of limit shapes L^{dumb} , which denotes two prolates sitting on top of each other, in this region of the phase diagram. As M. Wortis has pointed out to us, such a shape is unstable with respect to an exchange of area and volume (see Ref. [39]).
- [36] If the interaction between the membrane segments is attractive, a similar boundary condition applies as well for the adhesion of vesicles to a wall considered in Ref. [28]. Likewise, transitions arise between shapes which self-adhere and those which do not.
- [37] U. Seifert, *J. Phys. (Paris) Colloq.* **51**, C7-339 (1990); *Phys. Rev. Lett.* **66**, 2404 (1991).
- [38] W. Wiese and W. Helfrich, *J. Phys. Condens. Matter* **2**, SA329 (1990).
- [39] L. Miao, B. Fourcade, M. Rao, M. Wortis, and R. K. P. Zia, *Phys. Rev. A* **43**, 6843 (1991).
- [40] S. Svetina, V. Kralj-Iglic, and B. Zeks, (unpublished).
- [41] M. A. Peterson (unpublished).
- [42] For a review on the derivation of the elastic properties of the bilayer in terms of monolayer quantities, see A. G. Petrov and I. Bivas, *Prog. Surf. Sci.* **16**, 389 (1984).